DISSERTATION

EXTENDING SINGLE MOLECULE SPECTROSCOPIC TECHNIQUES TO MULTI-PARTICLE SYSTEMS OF SEMICONDUCTOR NANOCRYSTALS

Submitted by

Douglas Parker Shepherd

Department of Physics

In partial fulfillment of the requirements

For the Degree of Doctor of Philosophy

Colorado State University

Fort Collins, Colorado

Summer 2011

Doctoral Committee:

Advisor: Martin Paul Gelfand
Co-Advisor: Alan K Van Orden

Jacob Lyman Roberts
Amy Lucia Prieto

ABSTRACT

EXTENDING SINGLE MOLECULE SPECTROSCOPIC TECHNIQUES TO MULTI-PARTICLE SYSTEMS OF SEMICONDUCTOR NANOCRYSTALS

This dissertation describes the application of single molecule spectroscopic techniques to individual semiconductor nanocrystals (NCs), small clusters of NCs, and NCs used as the light harvesting layer in sensitized solar cells. We first examine how coupling between close-packed NCs may alter their photophysical properties by studying isolated NCs and small clusters of NCs via single molecule time-correlated single-photon counting, from which fluorescence intensity trajectories, autocorrelation functions, decay histograms, and lifetime-intensity distributions have been constructed. These measurements confirm that NC clusters exhibit unique photoluminescence behavior not observed in isolated NCs. In particular, the NC clusters exhibit a short-lifetime component in their photoluminescence decay that is correlated with low photoluminescence intensity of the cluster. A model based on non-radiative energy transfer to NCs within a cluster that have smaller energy gaps, combined with independent blinking for the NCs in a cluster, accounts for the main experimental features. This energy transfer may lead to energy sinks when an excitation is transferred to a NC that is in the *off* state. We then examine a model photovoltaic system where a sub-monolayer film of NCs is chemically coupled to a single crystal semiconductor (TiO_2 or ZnO) substrate through a variety of capping ligands. Again, utilizing time-correlated single photon counting and internal photon conversion efficiency we have studied both the photoluminescence intensity, photoluminescence decay time, and sensitized photocurrents. We find that for all configurations of capping ligands

and substrate the photoluminescence decay rate is quenched compared to the free NCs in solution; whereas, only the short chain capping ligands that promote electron coupling to the substrate produce photocurrents. The longer chain capping groups both inhibit the electron injection and promote NC clustering on the surface where interactions between the individual NCs or the NCs and substrate alter the radiative rate. This result confirms that the possibility of NC clusters leading to a loss of energy due to inter-NC coupling is present in devices and warrants further study.

Acknowledgments

I would like to take a brief moment to thank a few people without whom this dissertation would not be possible. First and foremost, my extremely patient wife, Alison Shepherd, who has supported me both emotionally and financially, allowing me to pursue my degree and love of the mountains simultaneously. I am thankful to my parents, Joseph and Donna Shepherd, for encouraging me to return to school, their support, and love. There are too many people I need to thank at CSU to all fit here, but three friends in particular, Shannon Riha, Justin Sambur, and Mark Sweeney have provided me with endless advice and guidance in areas outside of my expertise, particularly Shannon. Justin and I have had a fruitful collaboration, which resulted in the final chapter of this dissertation. My two advisors, Dr. Gelfand and Dr. Van Orden have provided excellent guidance and the oppportunity to indulge my passions outside of the laboratory. My committee members Dr. Jacob Roberts and Dr. Amy Prieto have supported me through the occasionally difficult process of living as a physicist among the chemists. The Van Orden lab has been a wonderful place to work, starting with tutelage under now graduated Keir Forgatory, Ming Chen, and Jeffrey McPhee followed by many hours of shared hardship and work with Kevin Whitcomb, Kenneth Milligan, Rajesh Nayak and Jon Gerding. Finally, Dr. Peter Goodwin at Los Alamos National Laboratory taught me more tricks about single molecule spectroscopy in our few months of working together than I learned in my previous four years of graduate school. I am deepy indebted to him for his help and looking forward to continuing working together as I transition to a postdoctoral position at LANL.

TABLE OF CONTENTS

List of Tables

List of Figures

List of Abbreviations

ACF	autocorrelation function
AFM	atomic force mircoscopy (microscope)
APD	avalanche photodiode
APTES	aminopropyltriethoxysilane
CW	continuous wave
DNA	deoxyribonucleic acid
ET	electron transfer
FLID	fluorescence lifetime intensity distribution
FRET	Förster resonant energy transfer
FWHM	full width at half maximum
IPCE	incident photon to current efficiency
IRF	instrument response function
MPA	mercaptopropionic acid
MUA	mercaptounedecanoic acid
NA	numerical aperture
NC	semiconductor nanocrystal
OA	oleic acid
ODA	octadecylamine
PCH	photon counting histogram
PL	photoluminescence
QD	quantum dot
QDSSC	quantum dot sensitized solar cell
R6G	rhodamine-6g
RNA	ribonucleic acid
SEM	scanning electron micrograph
SNR	signal to noise ratio
TA	transient absorption
TCSPC	time correlated single photon counting
TEM	transmission electron micrograph
THz-S	terahertz spectroscopy
TOPO	trioctylphosphine oxide
TPCH	true photon counting histogram
trPL	time resolved photoluminescence
SMS	single molecule spectroscopy

Table 1: Abbreviations used throughout this dissertation.

1 Introduction

Isolating, studying, and understanding an individuals' contribution to the overall properties of a group is a common theme throughout the history of science. In the Van Orden laboratory, we are specifically interested in understanding the role of individual fluorescent molecules and particles in a variety of environments—from simple systems, such as isolated molecular dyes in water, to complex systems, such as coupled colloidal semiconductor nanocrystals used as the active layer in a photovoltaic devices. The main goal of this dissertation is to elucidate our successes and shortcomings using a "bottom-up" approach to studying these systems, combining various techniques that fall under the general umbrella of single molecule spectroscopy (SMS) with intelligent sample design and simple theoretical modeling to gain information on time scales and complexity scales typically inaccessible to traditional SMS.

The fluorescent particles we will focus on for this work are spherical colloidal semiconductor nanocrystals or quantum dots, so called because of both their small size ($r \lesssim 5$ nm) and their photophysical properties that mimic single quantum emitters such as molecular dyes [1, 2]. As all of the nanocrystals in this work are quantum dots, we will interchangeably use the abbreviaions NC and QD. NCs are of great interest in many fields of research, including but not limited to biological imaging[3–6], lasers[7–11], photodetectors[12, 13], and photovoltaic devices[14, 15]. Typically consisting of a few thousand atoms of III-V (e.g., InAs) or II-VI (e.g., CdSe) materials, a high degree of composition and size control, as well as large yields, are possible utilizing colloidal synthesis techniques[1, 2, 5, 16–19]. To keep the final product stable and soluble in the chosen medium, ligands are bound to the surface. For solubility in or-

ganic solvents, typical ligands include trioctylphosine oxide and octyldecylamine; and for water solubility, typical ligands are mercaptopropionic acid and mercaptounedecanoic acid. These ligands are not physically isolated from the quantum dots: for instance, the thiol-terminated ligands that are used for water solubility quench the photoluminescence[20]. A thorough examination of both the physical and photophysical properties of quantum dots can be found in Chapter 2.

The initial push to achieve the necessary signal-to-noise to resolve emitted photons from a single fluorophore came mainly from two groups, Moerner's at Stanford University and Keller's at Los Alamos National Labs, with different motivations. The Moerner group was interested in determining how single fluorophores embedded in a heterogeneous sample of glass were affected by their local environments[21] and the Keller group was interested in developing a tool for analytical chemistry at the single molecule level[22]. As the technique developed, other groups began to utilize the capability to measure the individual photophysical properties of molecules. Specifically, the Weiss group at the University of California Berkeley showed that fluorescence resonant energy transfer could be measured at the single molecule level, allowing for dynamical measurements in heterogeneous populations where homogeneous populations are impossible to prepare[23]. Since then the field has exploded, utilizing the increased signal-to-noise available from SMS techniques to investigate a wide variety of individual fluorophores.

The time scale and length scale of various schemes to achieve single molecule resolution range from nanosecond timing resolution for photoluminescence lifetime measurements[24, 25] to specialized techniques that provide localization of individual fluorophores to less than nanometer (such as stochastic optical reconstruction microscopy)[26, 27]. All of these schemes are designed to extract the maximum signal-to-noise from the small number of photons that a single fluorophore emits. In contrast, ensemble spectroscopic techniques rely on a large number of photons to

isolate small signals, such as transient absorption spectroscopy, which has been used to measure transition times between higher energy levels in NCs[11, 28–30]. Ensemble techniques inherently average over all the individual fluorophores and the local environments that effect those fluorophores, providing a large amount of information that represents the behavior of the system as an average. The spectral and time resolution of ensemble techniques continues to improve, recently providing femtosecond resolution of the time evolution of excited states in PbS NCs[29]. The major contribution from ultra-fast ensemble techniques to the NC field is arguably the study of multiple exciton generation and the understanding of multi-body processes in NCs that has resulted from it[30].

To recap, SMS techniques allow for high signal-to-noise measurements and spatial localization of rarely emitting sources, such as individual, isolated NCs, while ensemble techniques provide ultra-fast time resolution for both common and rarely occurring processes by sampling many emitting sources. There exists a gap between these two experimental techniques, specifically experiments that can extract information on the time evolution of a system that is more complex than a single emitter, but is simple enough that the effects of local environment are measurable. Our interest in these time and complexity scales came about because of experiments initially performed by Dr. Ming Chen while she was a graduate student in the Van Orden group. She examined small clusters of CdSe/ZnS core/shell quantum dots under continuous excitation with scanning confocal microscopy and found that the characteristic blinking behavior was clearly different from that of small groups of isolated NCs[31]. To understand the underlying physical process which leads to this unique behavior of small clusters of NCs, we sought to further investigate the phenomenon by measuring the photoluminescence decay and attempt to construct a theoretical model with the new information gained.

We begin this dissertation with an overview of the physical and photophysical

properities of collodial semiconductor NCs along with single molecule spectroscopic techniques. We find that spherical core-shell NCs within close proximity communicate with each other, leading to the creation of "energy sinks" where photo-excited carriers may recombine on a timescale faster than radiative recombination or charge transfer. This result has implications for NC based devices, particularly photovoltaics where any pathways that compete with harvesting charge carriers decreases the efficiency of the device. By investigating a model photovoltaic system consisting of spherical NCs coupled to single crystal semiconductor substrates, we find evidence that spectroscopic confirmation of charge transfer in this system may actually be due to interactions between NCs in close proximity.

2 Colloidal Semiconductor Nanocrystals

Colloidal semiconductor nanocrystals are small crystals of semiconductors[1, 2], with typical diameters between 1-10 nm, coated with a surface ligand that provides solubility in either aqueous[5, 32] or organic[16, 18, 19] medium. For the majority of the work discussed here, the core of the NC is coated with a few monolayers of a semiconductor with a wider band gap, for example CdSe overcoated with ZnS, to provide surface passivisation and therefore more stable fluorescent properties[33, 34]. Both core and core/shell types of NCs are illustrated by the cartoons in figure 1. The ability to synthesize highly monodisperse solutions of high quality core/shell NCs with a variety of ligands is indicative of how far the synthetic control over NCs has come since the first reported works in 1993[1]. Given a particular synthesis, the final product may be drop-cast or spin coated onto a substrate to create an optically active thin film [35–37], diluted and deposited onto substrates suitable for SMS measurements,[31, 38–42] or introduced into biological systems as fluorescent probes[3, 6, 43]. To highlight this flexibility and importance of the advancements in colloidal synthesis, we refer the reader to Chapter 5 on quantum dot sensitized solar cells.

2.1 Colloidal Synthesis

Synthetic control over the size, composition, and surface ligand of semiconductor NCs is a key reason that NCs have emerged as the forerunner for a variety of applications in the nanoworld. While the focus of this work is on the photophysical properties of semiconductor NCs, a brief overview of NC synthesis is necessary because the quality of the surface plays a large role in determining these properties.

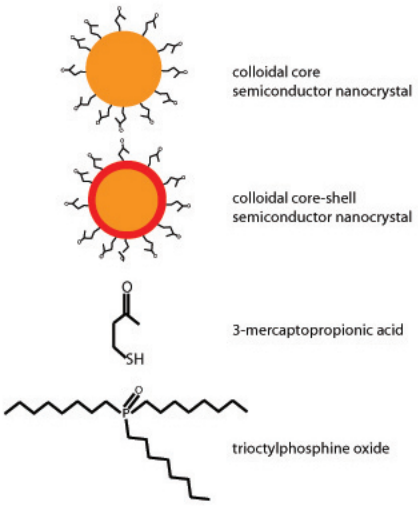

Figure 1: Core and Core-Shell Colloidal Semiconductor Nanocrystals
Cartoon of a (A) CdSe core nanocrystal with a bi-functional thiol ligand (MPA) and a (B) CdSe/ZnS core/shell nanocrystal with a bulky organic ligand (TOPO). The MPA capping ligands confers water solubility and chemical functionality while the TOPO ligand confers solubility in organic solvents and chemical isolation from the environment.

The typical synthesis for colloidal semiconductor NCs consists of three components: precursors, organic surfactants, and solvents. The three components are heated to the point where the precursor materials break down into their active molecular species that then nucleate and grow NCs, mediated by the surfactant molecules[16, 18, 44]. Because of the high surface-to-volume ratio (up to half of the atoms may be present at the surface of the NCs), control over the NC-ligand interface is key to high quality NC synthesis[19, 45, 46]. Figure 2 outlines a typical synthetic procedure for TOP-capped CdSe and CdSe/ZnS NCs.

Bulky organic ligands such as trioctylphosphine oxide and octydecylamine are typical choices for synthesis of semiconductor NCs that require both high photo and physical stability over time. However, these ligands are limited to use in organic solvents and have low binding energies, such that excess ligand must be present in the solvent to keep the NCs in solution. The advantages of bulky organic ligands are that they isolate the surface of the NCs from the surrounding environment and

do not interact with the excited state carriers[46–48]. Thiol-terminated ligands are currently the best choice to confer water solubility to NCs but unfortunately quench the photoluminescence[45, 46].

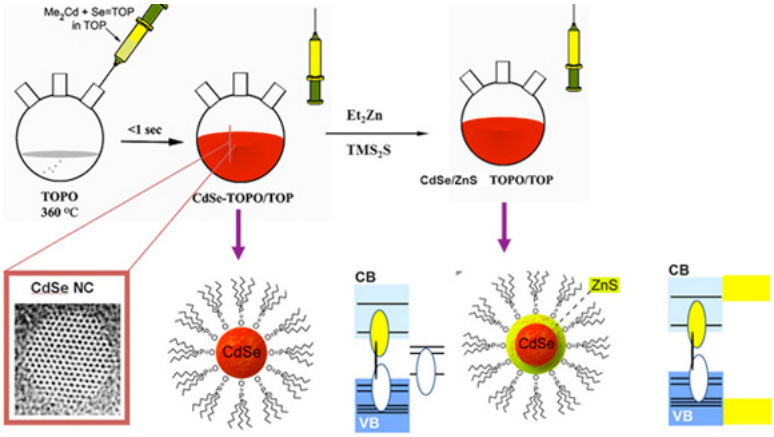

Figure 2: One Pot Colloidal Synthesis of Semiconductor NCs
Flowchart for a common synthetic approach process for high quality organic soluble semiconductor nanocrystals.

Even with high-quality synthesis there exist trap states at the surface of the nanocrystal because of the abrupt termination of the crystal lattice. The popular method to passivate these states is to grow a shell of material with larger band gap that has a small lattice mismatch with the core material, such as ZnS shell for a CdSe core[33, 34]. The photoluminescence quantum yield is typically raised from ≈10% for core only NCs to >50% for core/shell NCs[33]. This impressive increase has paved the way for core/shell NCs to take the place of organic fluorophores, because in addition to high quantum yields NCs are more resistant to photo-bleaching and have a host of other photophysical advantages, discussed in section 2.3.

2.2 Quantum Confinement

The simplest view of the quantum mechanical properties of semiconductor NCs is that of a three dimensional infinite square well potential which is discussed at length in introductory quantum mechanics courses. There exists a simple inverse dependence on the size of the well on the energy levels:

$$E_{n_x,n_y,n_z} = \frac{h^2}{8m}\left[(\frac{n_x}{L_x})^2 + (\frac{n_y}{L_y})^2 + (\frac{n_z}{L_z})^2\right] \tag{1}$$

This leads to a increase in the energy between levels as L_x, L_y, and/or L_z decrease in size. Figure 3 is a cartoon of how the energy levels near the band edge change as a semiconductor is size confined. This simple case can be extended to a particle in a spherical infinite potential, and utilizing the parabolic band-approximation one can express the energy levels as (note these energies are relative to the band extrema in an infinite crystal),

$$E_{l,n}^{e,h} = \frac{\hbar^2\phi_{l,n}^2}{2m_{e,h}r^2} \tag{2}$$

where l is the angular momentum quantum number, $\phi_{l,n}$ is the nth root of the spherical Bessel function, $m_{e,h}$ is the electron or hole mass respectively, and r is the nanocrystal radius. In an actual NC, the potential is finite, with steps at any interface, such as the core-ligand interface[48, 49]. This creates a finite probability that the particle exists outside of the NC, depending on the offset between the internal potential and the external potential. This allows for the individual charge carriers to tunnel from the NC to other NCs or appropriate acceptors, which is the basis for many NC devices.

An important length scale which helps understand the degree of quantum confinement is the Bohr radius of the bulk exciton,

$$r_B = \frac{\epsilon\hbar^2}{\mu e^2} \tag{3}$$

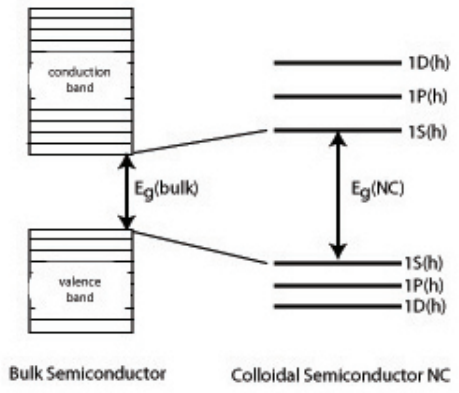

Figure 3: Size Dependent Energy Gap

Cartoon representation of the band gap and energy level size dependence in semiconductor nanocrystals.

where ϵ is the dielectric constant of the semiconductor and μ is the reduced electron-hole mass[2, 16, 18, 47, 49, 50]. When $r \ll r_B$, the NC is in the strong confinement regime. This is the situation for all of the NCs utilized in this work and as such we refer the reader to other works for discussions of the weak ($r \gg r_B$) and intermediate ($r \approx r_B$) regimes[16, 18].

In the strong confinement regime, the Coulomb interaction between the electron and hole lowers the energy of transitions only slightly and the electronic levels for both the electron and hole are quantized near the band edge. The energy required by an incoming photon to create an electron-hole pair is given by[16, 18]

$$\hbar\omega = E_g + E_v^h(r) + E_v^e(r) - \frac{1.8e^2}{\kappa r} \tag{4}$$

where E_g is the bulk band gap and $E_v^{(h,e)}(r)$ are the size dependent energy contributions from the hole and electron, leading to a distinct optical spectra, shown in figure 4, which shows a clear optical transition at the 1st exciton, but due to heterogeneous broadening from size and shape dispersion it is difficult to determine other distinct optical transitions at room temperature[51]. At low temperature, the Bawendi group

has recorded spectra of individual CdSe and CdSe/ZnS NCs that show the intrinsic emission linewidth of NCs is quite narrow (on the order of 0.1 nm), but as the temperature rises, homogeneous broadening from phonon coupling widens the emission spectrum[39, 52]. Additionally, only the states near the band edge are clearly quantized and at higher energy levels the transitions become closer to bulk like, leading to the near continuous nature of the absorption spectrum above the 1st exciton peak[29].

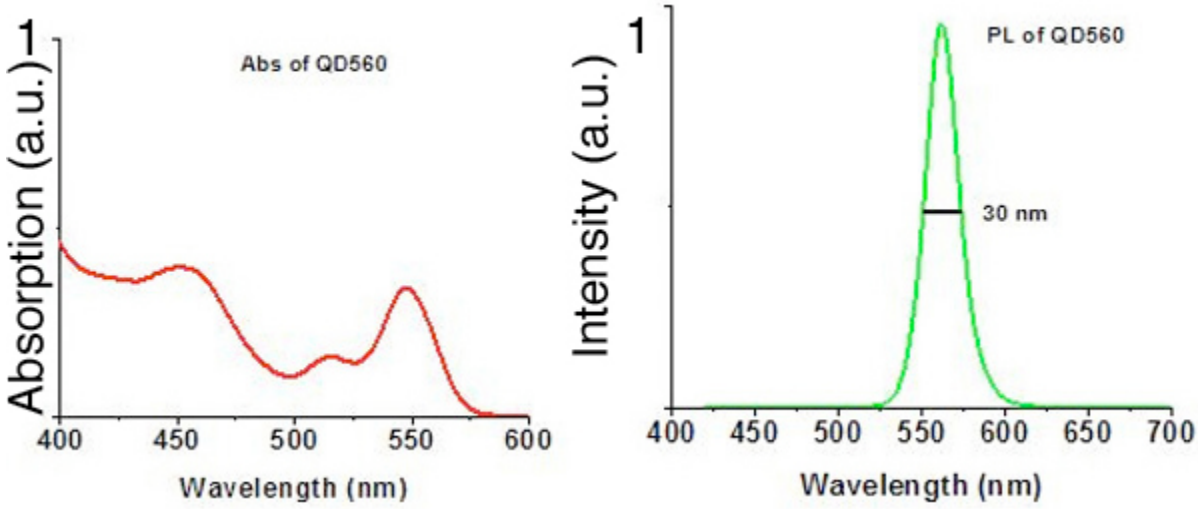

Figure 4: Absorption and Photoluminescence Spectra of an Ensemble of CdSe/ZnS NCs

Ensemble absorption and photoluminescence spectra of Ocean Nanotech CdSe/ZnS NCs provided by Ocean Nanotech.

2.3 Excited State Processes

The spectral features of semiconductor NCs are very different from molecular dyes, due a few key differences in the photophysics. Molecular dyes undergo a conformational change when a photon is absorbed, which have specific energy ranges that limit the spectrum of photons that may excite the molecule, giving rise to the narrow absorption features of molecular dyes[53, 54]. Conversely, almost any photon with an energy higher than the band gap of a semiconductor NC can be absorbed[1, 29, 52, 55, 56]. For very high energy photons (relative to the band gap), it has been proposed that there are many available electronic states because only the states that lie near the band gap are quantized in energy[29, 57]. Due to quantum confinement, there exists a distinct band-edge state that an excited NC will rapidly relax to, subsequently relaxing to the ground state through either radiative recombination or non-radiative recombination, occurring on the nanosecond timescale for CdX(X=S,Se,Te) based NCs [47, 52, 58–61]. The rate of radiative recombination depends on not only the intrinsic properties of the material, but also on competing non-radiative decay pathways. These pathways can be either static or dynamic and are introduced by photobleaching, surface defects, bulk defects, ligand vacanies, and the overall quality of synthetic procedures[30, 42, 48, 62, 63]. For our purposes, the detection of emitted photons is the window into the excited state of individual NCs. We are concerned with the following:

- How long it takes the photon to be emitted after excitation (photoluminescence lifetime)
- Number of photons collected in set, consecutive time bins (typically 10 ms)

Figure 5 displays a typical photoluminescence decay histogram from CdSe/ZnS core-shell NCs obtained in the Van Orden laboratory.

A single exponential fits the decay curve well, indicating one characteristic emission timescale,

$$I(t) = Ae^{-t/\tau} \tag{5}$$

after deconvolution with the instrument response function[24].

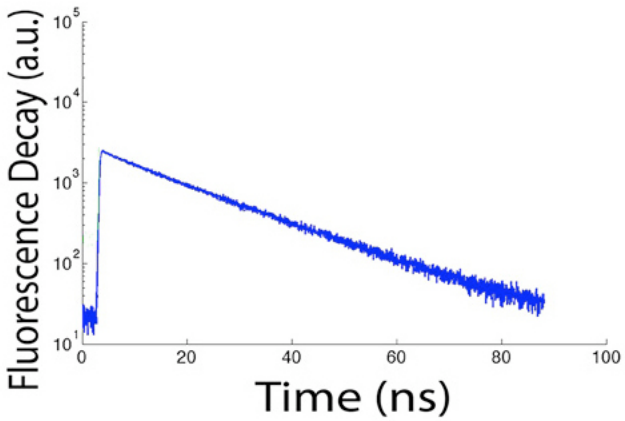

Figure 5: Photoluminescence Decay Curve From a Single CdSe/ZnS NC

Photoluminescence decay histograms (obtained in the Van Orden Lab) from CdSe/ZnS semiconductor NCs (synthesized by Ocean Nanotech) under pulsed excitation.

2.4 Fluorescence Intermittency

A key photophysical property of NCs went unnoticed until Nirmal first recorded the time-resolved photoluminescence from single CdSe NCs[38]. Individual semiconductor NCs display a characteristic time-dependent fluorescence under continuous-wave (CW) excitation, which switches seemingly at random between bright or "*on*" states to dark or "*off*" states. This phenomenon, known as blinking or fluorescence intermittency, has so far proved ubiquitous for various shapes (dots, rods, etc...) and material compositions (core, core-shell, double shell, etc...)[64, 65]. A typical fluorescence tra-

jectory for an individual NC is shown in figure 6, along with the photon counting histogram (PCH) that clearly shows two distinct intensity levels.

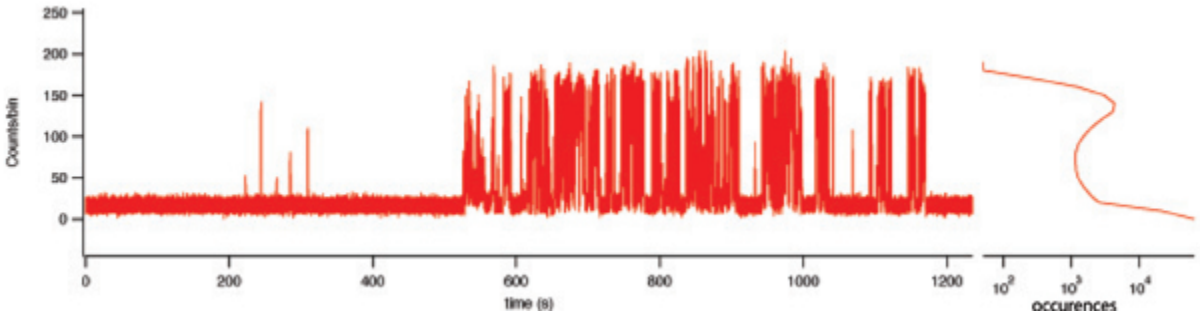

Figure 6: Fluorescence Trajectory From a Single CdSe/ZnS NC

Fluorescence trajectory (obtained in the Van Orden Lab) from a single CdSe/ZnS semiconductor NC (synthesized by Ocean Nanotech) under CW excitation.

By defining thresholds for both on and off, we are able to create on and offtime probability histograms, shown in figure 7a. Both of these histograms are well fit by a power law distribution,

$$P(t) = At^m \tag{6}$$

with m values of -1.5 and -1.7 for the *on* and *off* distributions, respectively. This inverse power-law dependence is well documented, beginning with Kuno's work in 2000[62, 66]. Extending this analysis to multiple generations of *on-on, on-off, off-off,* and *off-on* correlations provides a measure of the "memory" of the NC, or to put it another way, a measure of how random the *on/off* switching of the NC is[67, 68]. Figure 7b presents these four correlations for the fluorescence trajectory in figure 6. The lines are trend lines, displayed only to guide the eye as to the sign of the correlation. Phenomenological models have been proposed that are able to replicate the statisical properities of fluorescence intermittency, but the exact physical mechanism that governs blinking in semiconductor NCs remains hotly debated[67, 69–72]. Efros has published a thorough and well-written review in Nature Materials[65] which examines the possible physical mechanisms and issues associated with each. In this work,

we will not attempt to explain the exact nature of blinking, but we will utilize its distinct characteristics combined with high signal to noise single molecule techniques to investigate the coupling of NCs to both other NCs and semiconducting substrates.

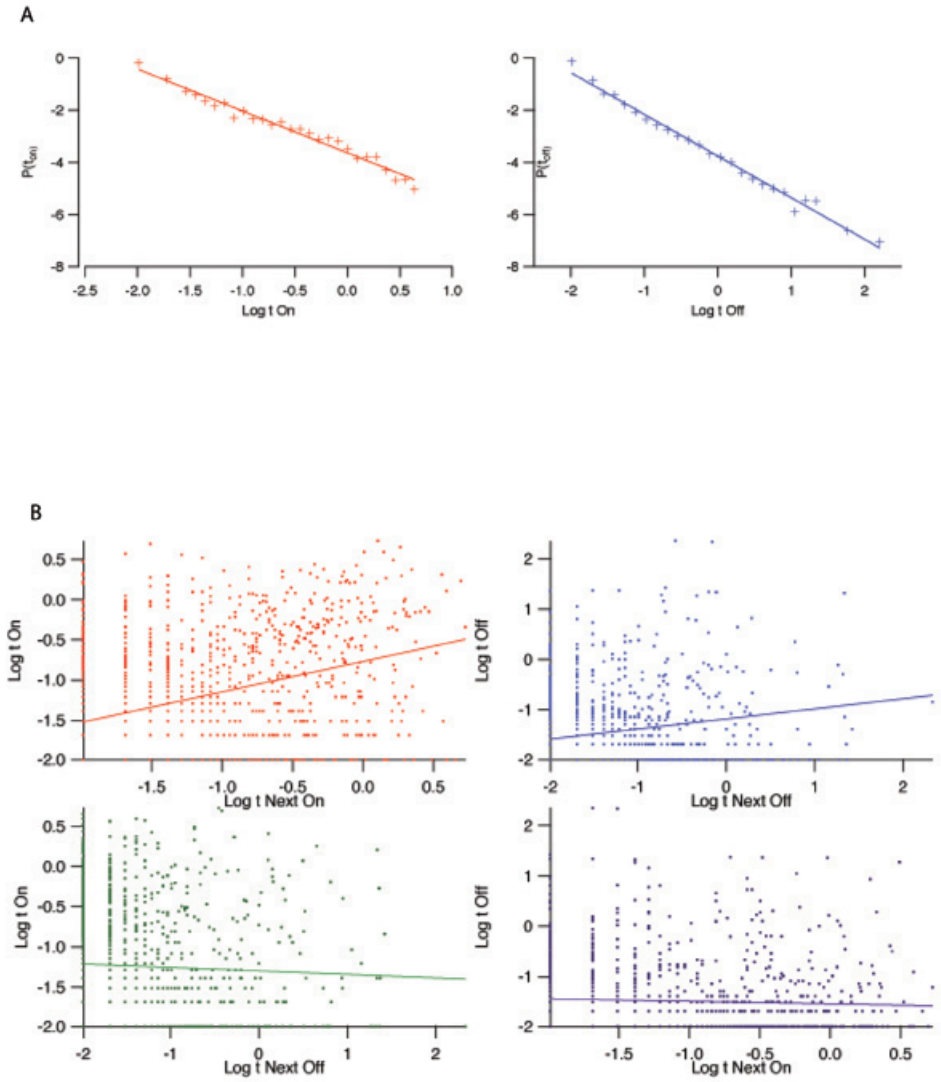

Figure 7: *On* And *Off* Analysis of a Single Semiconductor NC

Statistical *on-off* time analysis of the fluorescence trajectory shown in figure 6. A) *On* and *off* time histograms B) *on-on, on-off, off-on,* and *off-off* time histograms.

2.5 Inter-Nanocrystal Coupling

In isolation, semiconductor NCs have well defined physical and electronic properties. However, as NCs are brought into close proximity to each other, a variety of couplings are possible. At one extreme, chemically treated close packed thin films of CdSe NCs are almost completely coupled, allowing for excitations to be delocalized across many quantum dots[73–77]. At the other extreme, we have NCs that are completely decoupled and act indepenedntly. In-between, where NCs are in close (<10 nm) proximity to another NC, long-range resonant processes are possible[31, 35, 36, 78–82]. Förster resonance energy transfer (FRET) is a process through which an excited fluorophore, a NC in this work, transfers energy to an acceptor via dipole-dipole interactions[23, 83–86]. The relevant physical features which govern the rate, and therefore energy transfer efficiency,

$$F = \frac{1}{1 + (\frac{r}{R_0})^6} \tag{7}$$

of energy transfer is the distance between donor and acceptor where r is the center to center distance, and the Forster distance R_0, the distance at which the energy transfer efficiency is 50% is given by,

$$R_0^6 = \frac{9000 Q_0 (\ln 10) \kappa^2 J}{128 \pi^5 n^4 N_A} \tag{8}$$

where Q_0 is the quantum yield of the donor, κ^2 is the dipole orientation factor (often assumed to be random and equal to 2/3), n is the refractive index of the surrounding medium, N_A is Avogadro's number, and J is the spectral overlap integral. This last quanitity is given by

$$J = \int f_D(\lambda) \epsilon_A(\lambda) \lambda^4 \mathrm{d}\lambda \tag{9}$$

where f_D is the normalized donor emission spectrum and ϵ_A is the acceptor absorption spectrum, or molar extinction coefficient.

Biological systems spurred Förster to propose FRET and while the mechanism of FRET does not differ between the different types of fluorophores, the differences in basic photo-physics does play an important role in how FRET may be exploited[83]. As discussed above, molecular dyes have very narrow absorption and emission bands, with a Stokes shift that varies on the type of dye[87]. Semiconductor NCs have an extremely broad absorption band that lacks distinct features except at the first excitonic peak, yet have narrow emission bands[39]. These differences highlighted in figure 8 for rhodamine-6g versus a CdSe/ZnS NC.

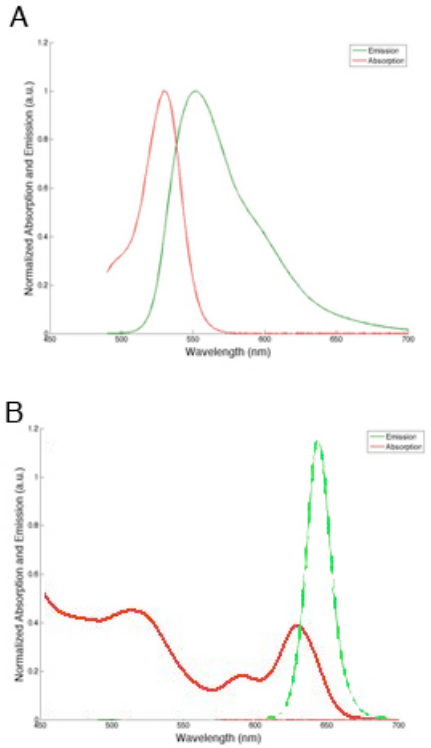

Figure 8: Absorption and Emission Spectra of R6G and CdSe/ZnS NC

Ensemble absorpton (red) and emission (green) spectra of A) Rhodamine-6G and B) CdSe/ZnS NC. Note the large overlap for the CdSe/ZnS NCs, especially for NCs that are blue-shifted (smaller in size) relative to this specific ensemble.

Because the efficiency of FRET is highly dependent on the spectral overlap (equation 9), we note that great care must be taken when utilizing molecular dyes because of the narrow spectral features. However, for semiconductor NCs, even the same size NC have large spectral overlap, allowing for FRET in systems that are fairly homogeneous. This is highlighted in experiments done by Koole *et al.* in which 1-D chains of CdTe NCs show different photoluminescence decay histograms from those in solution[81]. If different size NCs are used, then the donor species can be almost completely quenched, first shown by Kagan *et al.* with both homogeneous and heterogeneous size distributions of CdSe NCs coupled together in a thin film[78]. The tunability of quantum dots, coupled with synthetic flexibility and bio-compatible ligands has opened a whole field of new biological sensors based on FRET between NCs and molecular complexes[88].

2.6 Nanocrystal-Substrate Coupling

Given the size tunability and broad absorption of semiconductor NCs, they seem an ideal system to use as the active layer in light harvesting devices. A variety of schemes have been proposed to construct photovoltaic cells based on NCs[14, 15, 75, 77, 89–101], many based on the Grätzel cell configuration. The basic principle of the Grätzel cell is to split the photo-generated exciton into an electron and hole at an interface and harvest either one to do work (figure 9). Replacing the molecular dyes typically used in these devices with quantum dots has been moderately successful, achieving efficiencies up to 5%.

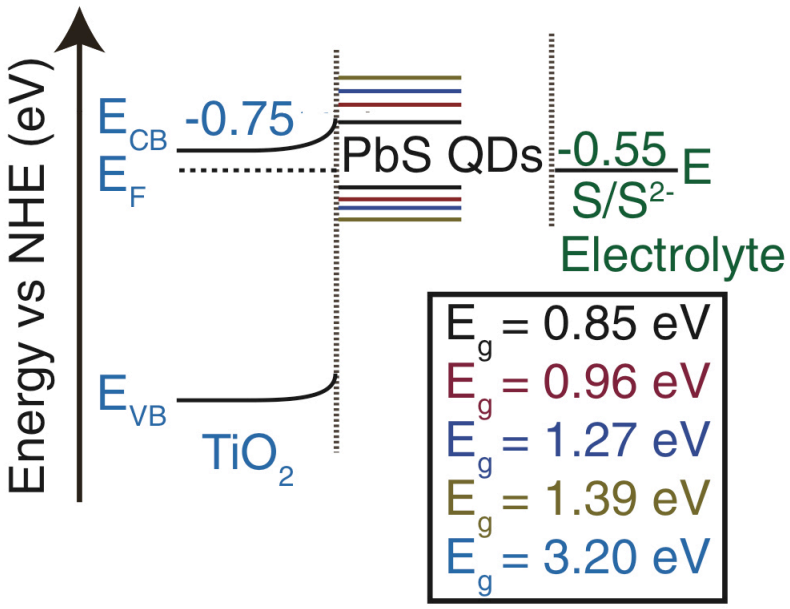

Figure 9: Energy Levels in a Quantum Dot Sensitized Solar Cell
Relative energy levels for a set of PbSe QDs with different energy gaps coupled to a TiO_2 substrate ($E_g = 3.20\,\text{eV}$). Not all QDs have the correct energy alignments for charge transfer. (Reproduced with permission from Justin Sambur[101]).

The efficiency of charge transfer between quantum dots and the electron accepting substrate, typically colloidal TiO2 nanoparticles, is one of the main factors in how efficient the devices will function as solar cells[29, 102–112]. There is some discrepancy in the literature regarding the rate of this process and in general a lack of

understanding of how the surface chemistry of both the NCs and substrate affects the process[104–106, 108, 110, 113]. If one naively assumes there are only two possible energy pathways for an excited NC coupled to an semiconducting substrate, radiative recombination or charge transfer to the semiconductor, it is possible to correlate the change in photoluminescence decay rate of NC coupled to a semiconductor to the native decay rate to determine the rate constant for charge injection. Utilizing this method, the Wise group has reported charge transfer on the 10-100 ns timescale from mercaptopropionic capped PbSe quantum dots to TiO2 nanoparticles[104]. However, Pijpers *et al.* report charge transfer on the 100 ps timescale for the same system by correlating photoluminescence decay, transient absorption, and terahertz spectroscopy with photocurrent measurements[110]. The Pijpers measurements obtain a charge transfer rate principally from the terahertz measurements, which actually measure the rise time of free carriers in the semiconducting substrate. Further discussion of these discrepancies can be found in Chapter 5.

3 Single Molecule Spectroscopy

Single molecule spectroscopy (SMS) is a field entering its third decade, during which rapid development has taken the state of the art from simply detecting the emission of single dye molecules in highly dilute solutions to investigating multiple fluorescent probes in a complex biological system simultaneously[114–116]. Our lab has mainly been interested in utilizing SMS techniques to achieve the necessary signal-to-noise for one or two probe region fluorescence correlation spectroscopy, investigating the conformational states of DNA/RNA hairpins labeled with molecular reporters[117]. In order to better understand a class of molecular reporters that Dr. Dale Willard developed consisting of bio-functionalized CdSe/ZnS quantum dots[88], we constructed a new microscope providing us with the following abilities:

- Scanning single molecule confocal microscopy[21, 22]
- Time correlated single photon counting[24, 118, 119]
- Atomic force microscopy registered with the confocal region[120]

While none of these techniques are new in the history of SMS, by combining them into a single platform we have been able to investigate new and novel systems that are not classically considered single molecule, but are also not ensemble systems. In the following sections we will outline how we attempt to utilize this capability to preform "non-ensemble spectroscopy"[31, 82].

3.1 Confocal Microscopy

The cornerstone of detecting fluorescence from a single molecule is reducing the background signal such that the SNR is high enough to distinguish the fluorescence both spatially and temporally. Patented by Marvin Minsky in 1961, confocal microscopy at first was conceived as an alternative method to conventional wide-field microscopy, with the advantage of filtering out background signal at the cost of losing any information which did not originate in the focal region, leading to reduced signal and longer exposure times. The confocal region is defined by the Rayleigh criterion,

$$R = \frac{.61\lambda}{NA} \tag{10}$$

where λ is the wavelength of the excitation light and NA is the numerical aperture of the microscope objective. Shown in figure 10a, R defines the distance from the central maximum to the first minimum of the laser intensity in the confocal area.

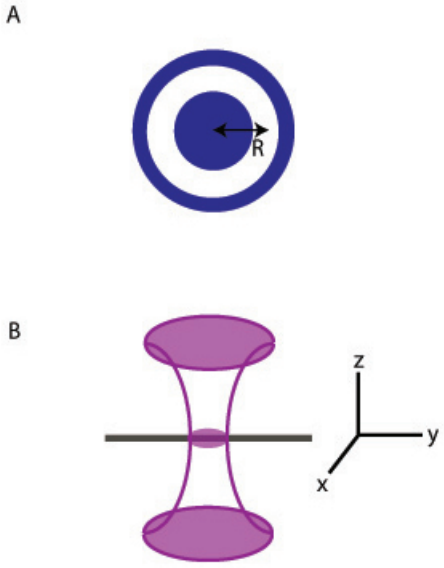

Figure 10: Confocal Region

Schematic view of the beam intensity in the confocal area looking from A) the top-down and the Rayleigh radius shown and B) a 3-D view that shows both the rapid focusing and expansion of the beam waist near the confocal region.

For high NA objectives (>1.0) and wavelengths in the visible (≈500 nm), this leads to an R of approximately 220 nm. Because the beam is so tightly focused, it rapidly expands in the x-y plane along the z-axis (figure 10b). To ensure that only light from the confocal region itself propagates to the detectors, a pinhole of diameter 50-75 μm is placed at the imaging plane of the microscope. An excellent review of pinhole selection can be found by Moerner and Fromm[21]. Further spatial reduction of the confocal region requires specialized techniques, such as exciting with a total internal reflection objective[121].

Because the confocal area is fixed and is small compared to the overall sample size, some sort of physical mechanism to move the focal area with high accuracy is necessary to do any sort of spatial imaging. Both laser scanning[122, 123] and physical scanning of the stage[21, 122, 124] are used to solve this issue, each of which has its own advantages. We utilize a high quality closed-loop piezo stage that provides nanometer scanning accuracy and precision, along with long-time stability. By scanning the sample, we are able to create a fluorescence map of any given area on the sample (figure 11). The stage can then be positioned at any area of interest with stability longer than our typical experimental collection times (hundreds of seconds). Due to NC blinking, multiple scans of a given area are usually required to obtain a complete fluorescence map. Once a NC of interest is centered within the confocal region, the input from the detectors is routed to a time correlated single photon counting board.

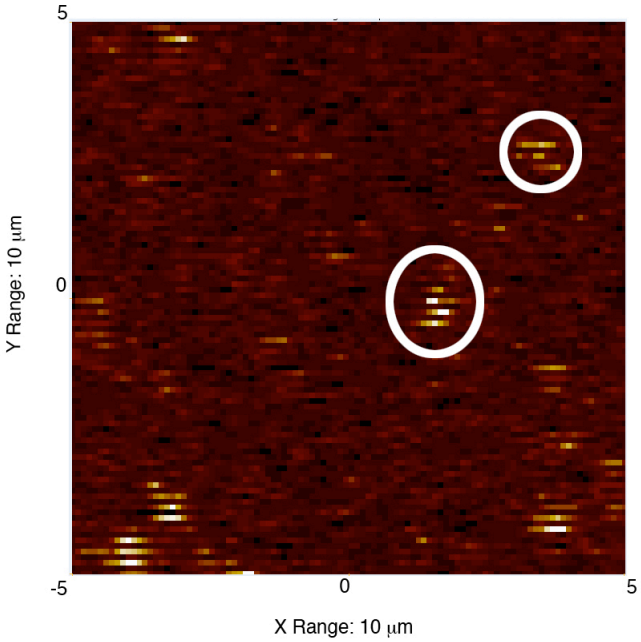

Figure 11: Fluorescence Map of CdSe/ZnS NCs Deposited on Mica
A 10×10 μm photoluminescence map of individual NCs and small NC cluster deposisted on a mica surface. The bright spots are intermittent because the NC are undergoing blinking while the stage is moving.

3.2 Time Correlated Single Photon Counting

Detecting a single photon from a single emitter is fairly trivial once the necessary signal-to-noise is achieved, as outlined in the previous section. Under continuous excitation, the only information available about photons arriving at the detectors is the arrival time from the beginning of the experiment, which is enough information to construct photon counting histograms, autocorrelation functions, and fluorescence trajectories. All of these processes allow for limited insight into the electronic state of the single emitter itself. A sample dataset from a single CdSe/ZnS NC obtained under CW excitation was shown in figure 6 from section 2.4.

Pulsed laser excitation and time correlated single photon counting (TCSPC) extend the scope of SMS experiments by taking advantage of the fact the single emitters are a rare photons sources compared to the pulse rate of the excitation source. Figure 12a outlines a typical pulse and photon train that generates a signal at the TCSPC electronics. The instrument response function (IRF, figure 12b) gives an overall characterization of the TCSPC system, because as individual components contribute to the timing error, the width of the IRF grows. A full review of how these components contribute to the overall timing resolution is discussed by Wahl[125]. By simply using statistical error propagation, we know that:

$$e_{IRF} \approx \sqrt{\sum e^2_{component}} \tag{11}$$

which tells us that the components with the largest timing error will contribute most to the overall system timing. In our experiments, the individual components that contribute to the full-width at half maximum (FWHM) of the IRF are:

- Avalanche Photodiode (APD) (Perkin-Elmer SPCM-14AQR)
- Pulsed Laser Source (Picoquant LDH-800)
- Time Correlated Single Photon Counting Electronics (Picoquant TimeHarp 200)

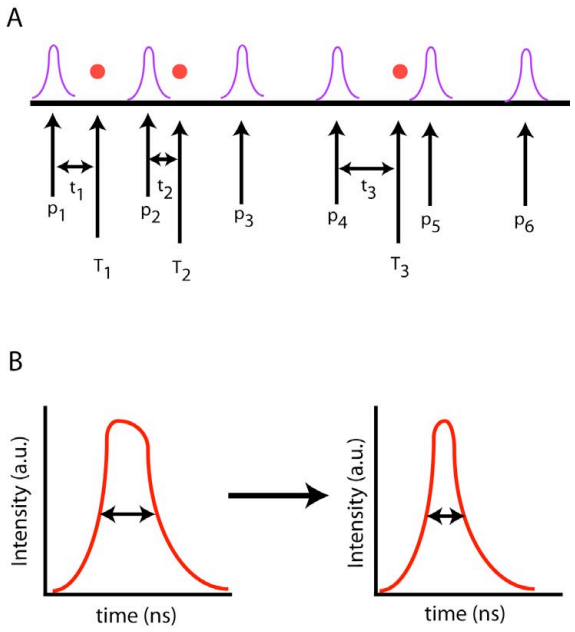

Figure 12: Photon Input Into the TCSPC Electronics

A) Schematic representation of the photon and pulse train arriving at the TCSPC electronics with the micro time label with lower-case "t" and the macro time label with upper-case "T". B) Relative size of the IRF for different system configurations and the absolute minimum width experimentally obtained.

The response time of the Perkin-Elmer APD is slightly less than a nanosecond, according to the manufacturer, the FHWM of the laser pulse generated by the Picoquant pulsed laser is ≈600 ps, and the timing jitter of the Picoquant TimeHarp 200 is ≈1 ns. The only piece of our system easily exchangeable are the APDs, which we have exchanged for Picoquant APDs that have sub-nanosecond timing jitter, but we are overall limited by the jitter of the TCSPC electronics. To fully utilize the impressive timing precision of TCSPC, the detectors must have time to reset in between photon arrivals. If more than one photon arrives per pulse, then it is more likely

that the photons arriving closer to the excitation pulse will be detected, skewing the experiments. To ensure maximum precision in our experiments, we tune the laser fluence such that we only excite one electron-hole pair in the semiconductor NCs and at most one emitted photon per pulse.

TCSPC has evolved over time and now is capable of recording the absolute arrival time, relative arrive time to the pulse, and the channel that individual photons arrive from. This allows for enormous flexibility in data processing, because it is possible to analyze the "macro" time elements such as autocorrelation functions while simultaneously analyzing the "micro" time elements including the average photoluminescence lifetime as a function of time (figure 13). We take advantage of this experimental flexibility in our lab by generating two-dimensional histograms that correlate macro-features to micro-features. One such correlation is a fluorescence lifetime intensity distribution[126](see figure 25 in Chapter 4 for an example). By binning the raw photon stream into 10 ms bins, the lifetime is plotted as a function of the total number of photons of each bin. Many types of such 2D histograms are possible, and by utilizing two detectors it is possible to generate higher dimensional correlations by filtering the emitted photons by wavelength or polarization.

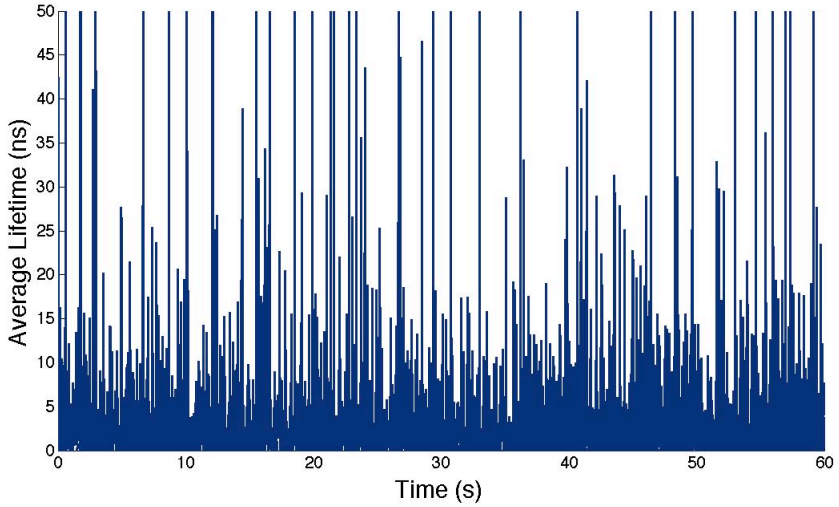

Figure 13: Fluorescence Lifetime Trajectory of a Single CdSe/ZnS NC
Average photoluminescence lifetime plotted as function of time. The average decay rate is calculated for each 10 ms bin, which leads to bins with small number of photon events having larger error.

3.3 Atomic Force Microscopy

Atomic force microscopy (AFM) is a technique that falls under the more general category of scanning probe microscopy. These techniques rely on some sort of probe, in the case of AFM a cantilever with a tip protruding from the end (figure 14), that interacts with the sample. By monitoring changes in the physical properties of the probe, information about the physical properties of the sample surface such as topography, electronic charge and polarizibility, occupied and vacant electronic states, magnetic properties, and more can be obtained[127–129]. We specifically use tapping mode AFM to spatially map the surface of our samples, with Ängstrom z resolution and approximately nanometer x/y resolution[128, 130].

A general AFM setup is outlined in figure 15. A diode laser is reflected off of the cantilever near the tip into a quadrant photodiode. In the simplest mode, contact mode AFM, the deflection of the cantilever is kept at a constant value by measuring the deflection with the laser and raising or lowering the cantilever via a feedback loop. For our purposes, principally finding single NCs on a surface, the drawback of contact mode AFM is that NCs may become stuck to the tip as it drags along the surface, ruining the measurement. We instead use tapping mode AFM, where the cantilever is oscillated near resonance by a piezoelectric motor. As the cantilever is scanned across the surface, the frequency of oscillation changes due to tip-surface interactions[128, 130]. Similar to contact mode, the laser is used to measure this change and the feedback loop attempts to maintain a constant oscillation frequency by altering the height of the cantilever. Lowering the amount of tip-surface interactions, and therefore the likelihood of a NC attaching to the tip, is not the only positive outcome from tapping mode AFM. By measuring the back-scattered light from the AFM cantilever, we are able to register the AFM tip to the confocal region.

Figure 16 outlines how we achieve this localization, which is essential to our experiments. As the AFM tip passes through the confocal region (figure 16b), light is

A

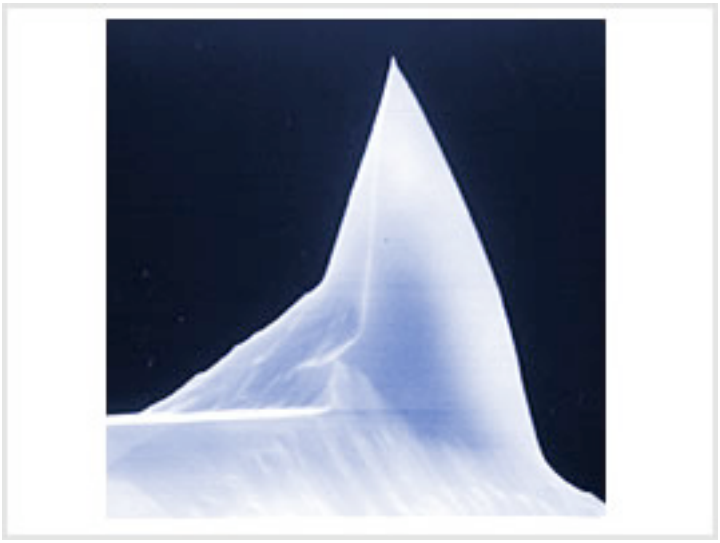

B

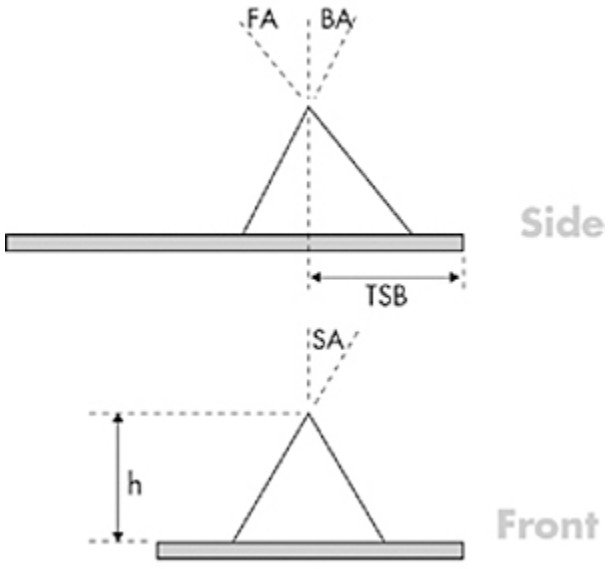

Figure 14: Overview of a Veeco TESP AFM tip (reproduced from Veeco AFM probes information)
A) SEM image of the Veeco TESP tips we use in our experimental setup. B) Schematic overview of Veeco TESP tips. h $= 10 - 15\,\mu m$, TSB $= 5 - 25 \mu m$, FA $= 25 \pm 2.5$, BA $= 15 \pm 2.5$, and SA $= 22.5 \pm 2.5$.

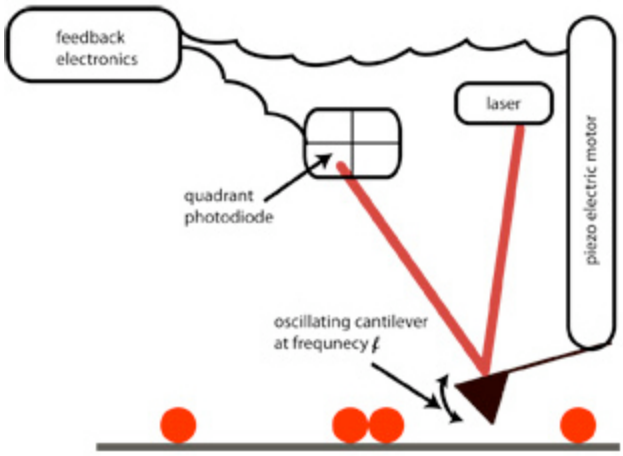

Figure 15: Side-View of AFM Feedback Loop

Schematic representation of an atomic force microscope scanning laterally across a surface with the various electronics and feedback loops indicated.

scattered at the frequency of the cantilever oscillation. This light is reflected offthe dichroic mirror inside the microscope and then directed through a series of lens and a pinhole to a photodiode. Here we use the same principles from confocal microscopy by spatially filtering the backscattered light with the pinhole to ensure that only light scattered by the AFM tip when it is in the confocal region reaches the photodetectors. The photodiode's output is passed to a lock-in amplifier that is using the oscillation frequency of the cantilever as a reference signal. The output of the lock-in is fed into the AFM controller (Digital Instruments Dimension IIIa) and simultaneously displayed alongside the topography information generated from the tapping mode AFM scan. An example scan is shown in figure 17, clearly displaying NCs both in and out of the confocal region.

From figure 17, one might conclude that we are able to distinguish single NCs from groups of closely-packed NCs. Unfortunately, because the radius of curvature of our AFM tips (Digital Instruments TESP) is approximately 20 nm, we are unable to spatially distinguish separate objects smaller than that. As mentioned above, the z-resolution is sub-nanometer because that information is dependent on changes in

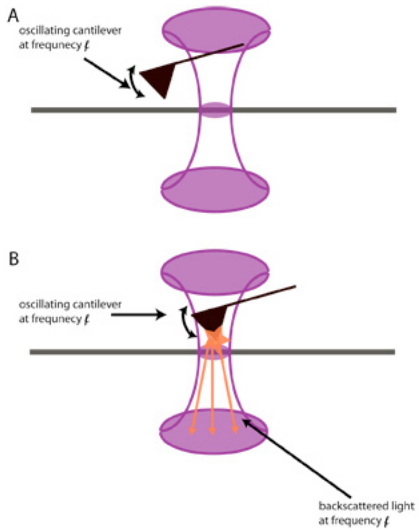

Figure 16: Cartoon of AFM Localization

As the AFM tip scans across the surface, it spends the majority of the time A) outside of the confocal area, with the only back-scatter coming from the cantilever. Once the tip B) enters the confocal region, the backscattered light is collected through the microscope objective. Note this schematic is not to scale, as the cantilever itself is microns long and the confocal region is approximately 0.5 micron in diameter. This drawing is not to scale, as the cantilever itself is 125 μm long and the confocal region is $\approx$ 500 nm across.

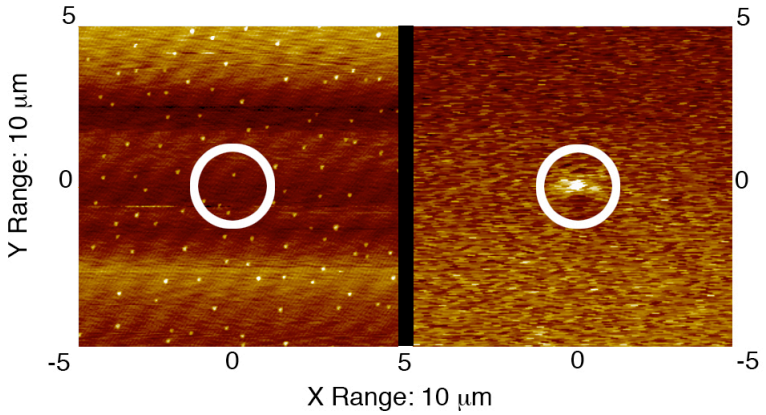

Figure 17: Correlated AFM Map and Confocal Region of CdSe/ZnS NCs on Mica Registered AFM image (left) and image of laser light scattered by the AFM tip as it pass through the confocal region (right). The confocal spot in this image is contained within the white circle and the corresponding area shown in the AFM image. In this particular image, there are a large amount of single NC and clusters of NCs. By adjusting the initial concentration and speed of the spin coater we are able to vary the surface coverage.

the resonant frequency and is nominally insensitive to the size of the tip. It is still possible to quantify the differences in physical features on length scale less than 20 nm by calculating the effective volume of the object. Figure 18 shows a line-cut of the height profile through the center of a single CdSe/ZnS NC, independently verified through TCSPC measurements. The effective volume is given by half the volume of a spheroid:

$$V = \frac{4}{6}\pi a^2 b \tag{12}$$

with a and b being the major and minor axes of the spheroid. This treatment has proved surprisingly rigorous, consistently provided a qualitative difference in effective volume between single NCs and clusters of NCs[31].

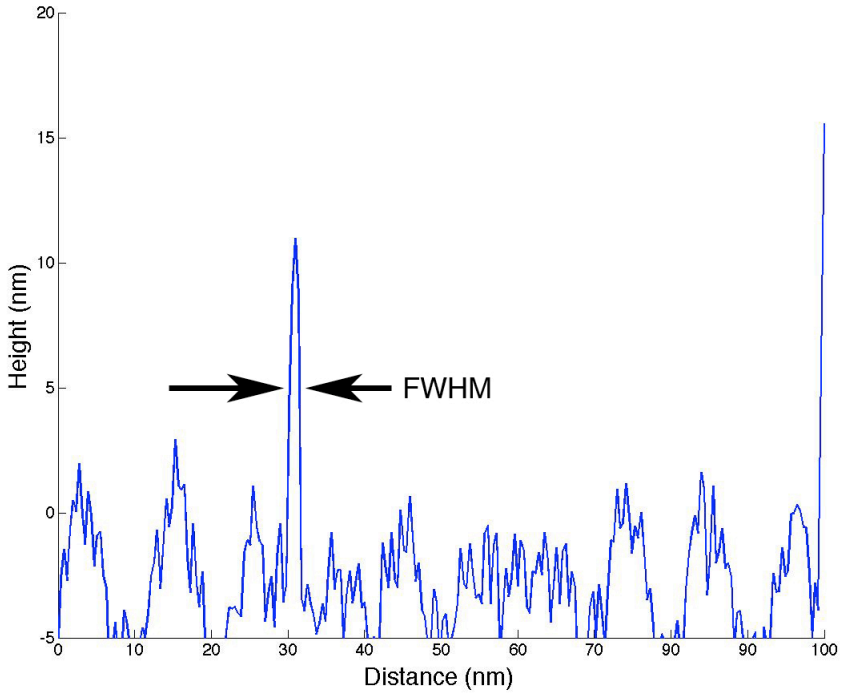

Figure 18: AFM Height Profile of a Single CdSe/ZnS NC on Mica
A line-cut from figure 17 across a single NC. The height is $\approx$ 10 nm and the FWHM is 1.5 nm. This gives an effective volume of $\approx$ 50 nm^3 according to equation 12.

3.4 Non-Ensemble Spectroscopy

A major goal of this work was developing a framework for spectroscopic measurements that allows us to probe systems that consist of more than one molecule or NC, such as a NC thin film, but still allow for quantitative measurements at the single particle level, such as anti-bunching, single particle photoluminescence decay, and fluorescence intermittency. By first studying individual NCs and small clusters of individual NCs, we probe how the photophysical properties of individual NCs are altered through NC-NC coupling. By correlating these changes and minimalist modeling, we are able to draw conclusions about how this coupling alters the timescale of emission from the NCs. Extending this knowledge to a model photovoltaic system of individual NCs and small NCs clusters coupled to semiconductor substrates, we are able to utilize the information gained from the original SMS measurements combined with new measurements to show that NC-NC coupling may effect the efficiency of devices. Only by studying the photophysical properties of individual NCs and small clusters of individual NCs with SMS measurements were we able to understand how the changes in photophysical properties of NCs coupled to semiconductor substrates arise.

4 Small Clusters of Colloidal Semiconductor Nanocrystals

The work in this chapter is published in *The Journal of Physical Chemistry C*[82]. Sections 4.5-4.8 provide additional information on both the work presented in the paper, follow-up theoretical work and data analysis. Matlab computer code and a tabulation of FLIDs is available at the Colorado State Libraries Digital Repository. All the experimental work was carried out by myself and Dr. Peter Goodwin at Los Alamos National Laboratories. The theoretical work and data analysis was performed by myself, Dr. Alan Van Orden, and Dr. Martin Gelfand. Kevin Whitcomb and Kenneth Milligan assisted with sample preparation. I am the primary author on the paper, with major contribution from Dr. Goodwin, Dr. Van Orden, and Dr. Gelfand. Kevin Whitcomb has continued with this project and is attempting to both measure the number of NCs in individual clusters and characterize the *on/off* behavior of NC clusters by measuring and analyzing fluorescence trajectories that are tens of minutes long.

4.1 Introduction

As noted earlier, individual and close-packed colloidal semiconductor quantum dots[1, 2] (QDs) form the building blocks for many established and promising nanotechnologies, such as biological labeling and imaging[131–134], photovoltaic devices[14, 113, 135], and other optoelectronic devices[13, 28, 136]. QDs have been studied extensively via both ensemble[63, 137–139] and single-molecule spectroscopic techniques[31, 42, 66, 70, 126, 133, 140, 141], such that the optical and electronic properties of

isolated QDs are reasonably well understood. However, many applications involve coupling QDs to other species, such as fluorophores[103, 132, 142, 143], electron donor/acceptors[103, 135, 144, 145], or other QDs[31, 35, 36, 81, 146–149]. This coupling may render the optical and electronic properties of the QDs partially or entirely altered. Studies that probe the consequences of such coupling interactions will provide fundamental knowledge to improve and control many QD-based devices.

Many groups have studied Förster resonance energy transfer (FRET), Dexter energy transfer, and electron transfer (ET) between QDs and various organic molecules [103, 132, 134, 142–144, 150], and these processes are becoming increasingly well understood. However, much less is known about the interactions of QDs with other QDs in close-packed systems. Studies have been reported on FRET in one dimensional QD chains, QD thin films and QD solutions;[35, 36, 81, 146, 147, 149, 151] however, all of these studies used ensemble averaging spectroscopic techniques to study the energy transfer. Furthermore, many of these studies used systems that were biased towards FRET due to the presence of different sized QDs[36, 147, 148, 151]. Our recently published work demonstrates that inter-QD interactions can be characterized through the study of small, close-packed clusters of nominally monodisperse QDs amenable to single-molecule spectroscopic techniques that do not average over the broad distribution of local environments that exist in bulk systems.

Previous single-molecule spectroscopic studies on QDs have been used to investigate the phenomenon of "blinking", the *on/off* switching of the fluorescence ubiquitous to almost all QDs[31, 42, 65, 66, 70, 133, 140, 152–154]. It is thought that the individual QDs that make up higher order structures also exhibit blinking. However, techniques that rely on ensemble averaging cannot determine the effect of blinking on the opto-electronic properties of these structures. Our group has used single-molecule spectroscopic techniques to study the fluorescence properties of both isolated QDs and small isolated QD clusters containing approximately two to ten similar sized CdSe-

ZnS core-shell QDs, such that blinking is still observable, under continuous wave excitation[31]. Other groups have carried out similar studies on both semiconductor nanocrystals[133] and nanorods[141]. In our group's original study, it was reported that such clusters exhibited strikingly different blinking behavior from both isolated single QDs and small groups of isolated QDs under simultaneous illumination. This behavior was denoted as "enhanced blinking" and speculated that it could be caused by interactions between neighboring QDs[31]. Lee and Maenosono addressed this idea in a theoretical study based on interactions of externally trapped charges[155].

To gain further insight into the photo-physical properties of higher order structures, particularly the interplay of fluorescence intermittency and energy transfer between individual QDs in the cluster, we carried out studies of CdSe-ZnS core-shell QDs and QD clusters using single-molecule time-correlated single-photon counting and pulsed-laser excitation. These measurements were combined with atomic force microscopy (AFM) to verify the presence of isolated QDs or QD clusters in the optical probe region (figure 19)[120]. On the basis of these results, we suggest that enhanced blinking is a consequence of independent blinking of the individual QDs and rapid energy transfer between QDs in the cluster[133, 152, 155]. Possible energy transfer mechanisms that may explain this observation are Förster resonance energy transfer or Dexter exchange, both of which are highly dependent on the inter-QD spacing and therefore cannot be distinguished using our measurements due to the limited lateral resolution of the AFM. Consequently, we will use the generic term "energy transfer" to refer to the interaction.

Our perspective is that the blinking of individual QDs leads to the creation of energy sinks in the cluster, which may have important consequences for higher order structures, such as thin-film QD based devices[13, 35, 36, 76, 136, 151, 156]. A simple kinetic model of energy flow between QDs is qualitatively consistent with experimental features such as the single-molecule fluorescence intensity trajectories, autocorrelation

functions, and fluorescence lifetime-intensity distributions. This work has provided novel insight into the mechanism by which individual QDs interact because of the ability to probe the relationship between blinking and fluorescence decay dynamics of the individual QDs and small QD clusters.

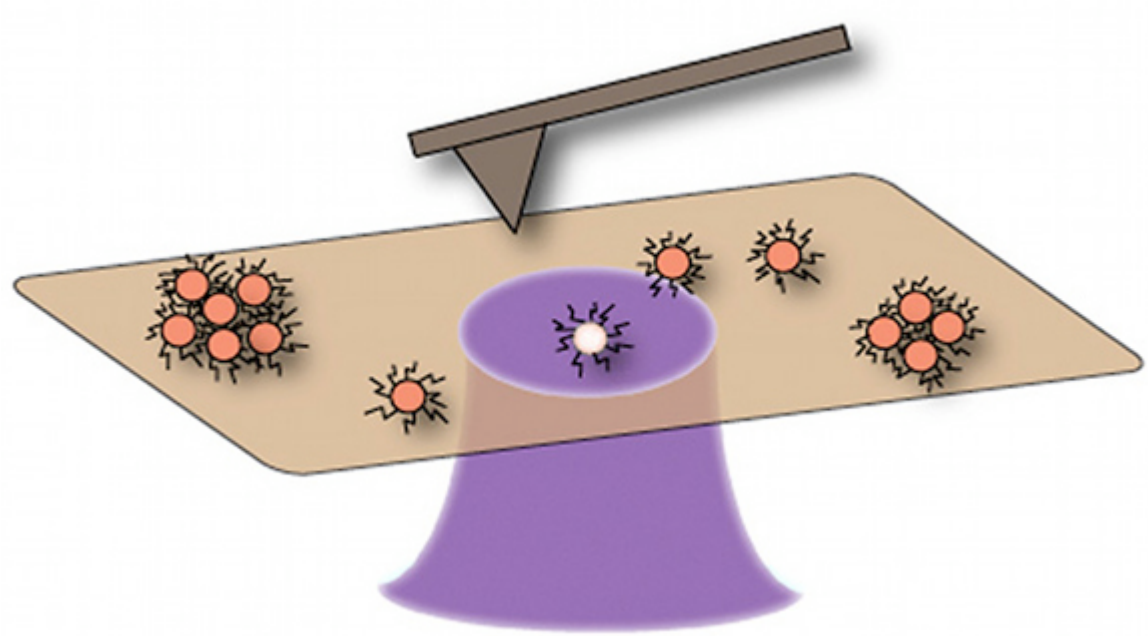

Figure 19: Experimental Setup

Diagram of the confocal probe region and AFM tip. The confocal region is spatially correlated with the AFM tip on the surface. The QDs are dispersed at a low surface coverage such that there is only one isolated QD and QD cluster in the confocal region.

4.2 Experimental Setup

The QDs examined in this study consisted of CdSe-ZnS core-shells, solubilized with shell bound octadecylamine ligands. The average core diameter of the QDs was 3.8 nm, corresponding to a peak emission wavelength of 560 nm. The QD samples were purchased from Ocean Nanotech (QSO-560-0010) in the form of 10 mg/mL solutions in toluene. Samples of individual isolated QDs were prepared by diluting 1 μL of

stock solution in 5 mL of toluene and spin casting 50 μL of the resulting solution on a APTES coated mica chip bonded to a glass microscope coverslip with optical epoxy. QD clusters were prepared by treating the diluted solution with 5 μL of methanol and allowing the mixture to stand for 15 min. Addition of methanol causes aggregation of the QDs due to interactions between the hydrophobic ligands. 75 μL of the resulting solution was then spin cast onto an APTES coated mica coverslip.

The mica coverslips were mounted on the stage of an inverted optical microscope (Olympus IX71) equipped with a piezoelectric scanner (Physik Instrumente P773.3CD XYZ) for positioning isolated QDs and QD clusters in the optical probe region of the microscope. Excitation was provided by a 440-nm pulsed diode laser (PicoQuant LDH-P-C 440) operating at a pulse repetition rate of 10 MHz and pulse width of ≈100 picoseconds. The laser light was focused onto the stage using a 1.4 NA/100× oil immersion microscope objective to form an approximately 0.5-μm-diameter optical probe region at the top surface of the coverslip. An average power of approximately 250 nW was used to give a time-averaged excitation intensity of approximately 30 W/cm^2, ensuring that we are only exciting one QD in the cluster during any given pulse, assuming an absorption cross section on the order of 10^{-16} cm^2[157]. Emitted fluorescence was collected by the same microscope objective and directed onto a single-photon counting avalanche photodiode detector (APD) (Perkin Elmer SPCM-14AQR). The emission was spatially filtered using a 75-μm-diameter pinhole located in the image plane of the microscope and spectrally filtered using a 40 nm bandpass filter centered at 562 nm before reaching the detector. The output of the APD was directed to a time-correlated single-photon counting module (PicoQuant PicoHarp 300) to record the photon data. The photon data was post-processed using vendor-supplied software (Picoquant Symphotime) to obtain fluorescence intensity trajectories, fluorescence decay histograms, and autocorrelation functions for each isolated QD and QD cluster.

An atomic force microscope (Veeco Instruments Bioscope SZ), mounted on the stage of the inverted optical microscope, was used to record nanometer scale topography images of the QDs and QD clusters occupying the probe region of the optical microscope. The images were recorded using Si nanoprobes (RTESP) operated in tapping mode with resonance frequency of approximately 300 kHz. Spatial alignment of the AFM tip with the optical probe region was accomplished by monitoring the excitation laser light scattered from the tip using a second APD.

4.3 Results and Discussion

The fluorescence trajectories for an isolated QD and a QD cluster are shown in figures 20 and 21, respectively. The insets in figures 20 and 21 show the corresponding AFM images of the particles being probed in each case and confirm, via effective volume calculations[31], that the particle in figure 20 is an isolated QD and that in figure 21 is a QD cluster.

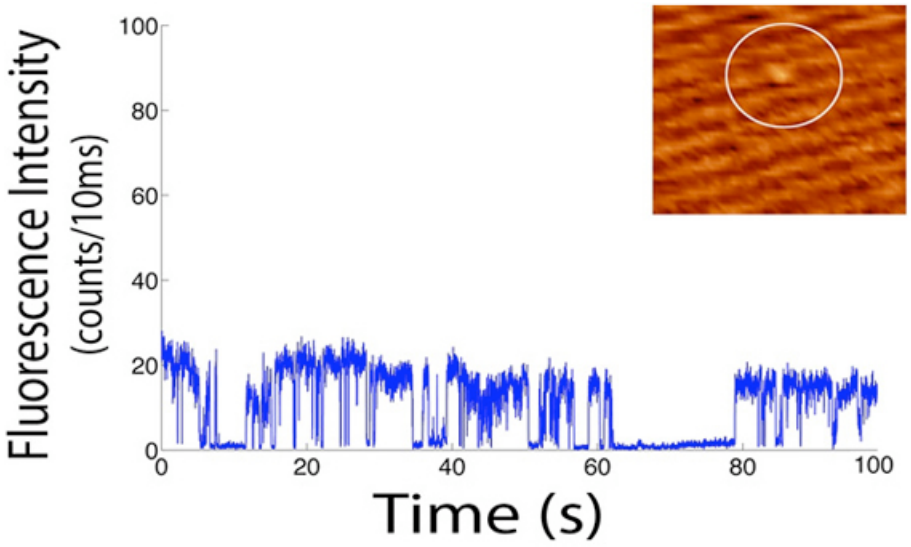

Figure 20: Fluorescence Trajectory From Single CdSe/ZnS QD

Isolated QD fluorescence trajectory; inset; isolated QD AFM image (500 × 500 nm, height scale 5 nm) with an effective volume 150 nm^3.

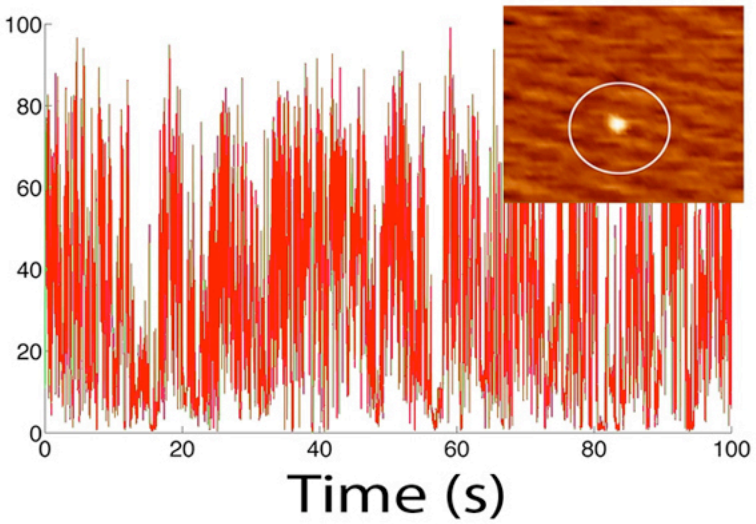

Figure 21: Fluorescence Trajectory From Cluster of CdSe/ZnS QDs

QD cluster fluorescence trajectory; inset: QD cluster AFM image (500 × 500 nm, height scale 5 nm) with an effective volume of 600 nm^3.

A notable difference in these trajectories is the much more rapid blinking in the QD cluster compared to the isolated QD. This behavior is consistent with the previously reported phenomenon of enhanced blinking[31]. A useful way to characterize the fluorescence trajectories is to calculate the autocorrelation function (ACF)[126]

$$g^{(2)}(\tau) = \langle \delta I(t) \delta I(t+\tau) \rangle / \langle I(t) \rangle^2 \tag{13}$$

shown in figure 22.

In eq 13, the angle brackets denote an time average, $I(t)$ represents the fluorescence intensity at time t, and $\delta I(t) = I(t) - \langle I(t) \rangle$. The isolated QD has a characteristic prolonged decay in the ACF, while the ACF of the QD cluster decays more rapidly. We quantify this behavior by defining a roll-offtime, τ_R, as the lag time at which the ACF decays to 50% of its value at $\tau = 10^{-2}$ ms (table 2).

Figure 23 displays the fluorescence decay histograms corresponding to the isolated QD and the QD cluster presented in figures 20 and 21. The fluorescence decay histogram of an isolated QD is dominated by a long-lived component. Assuming

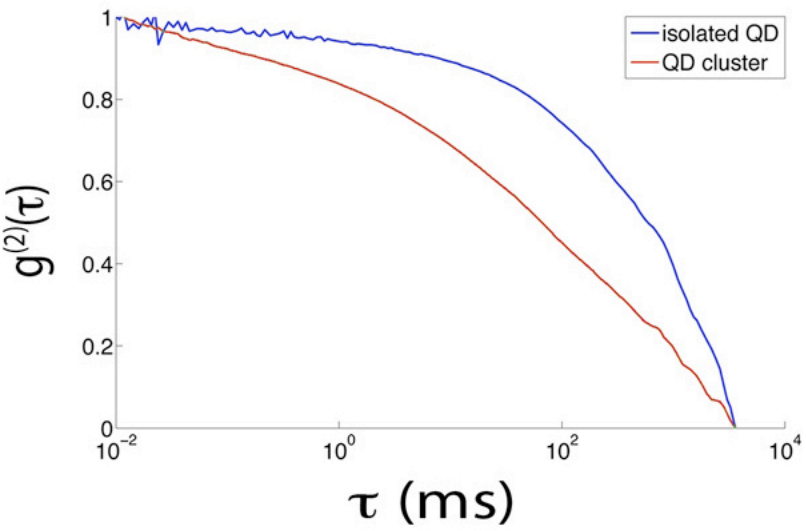

Figure 22: Autocorrelation Functions of Both an Isolated QD and QD Cluster

Fluorescence intensity autocorrelation functions from the isolated QD (figure 20) and QD cluster (figure 21) normalized at $\tau = 0.01$ms.

a collection of simultaneously illuminated, independently emitting QDs, one would expect the fluorescence decay of a QD cluster to be characterized by a superposition of similarly long-lived components[42]. Notably, this is not the case for the QD clusters observed in this study, for which the fluorescence decay is well described by a bi-exponential function

$$D(t) = Ae^{-t/\tau_1} + Be^{-t/\tau_2} \tag{14}$$

with a prominent short-lived component (τ_1) and a long-lived component (τ_2). The long-lived component is consistent with that of an isolated QD. The results of fitting the fluorescence decay histograms in figure 23 to eq 14, and correcting for the instrument response, are shown in table 2. For consistency, we have fit both isolated QDs and QD clusters to eq 14, allowing for direct comparison of the fluorescence decays. Ideally A is zero for isolated QDs, however there exist many possible explanations as to why A could be non-zero.

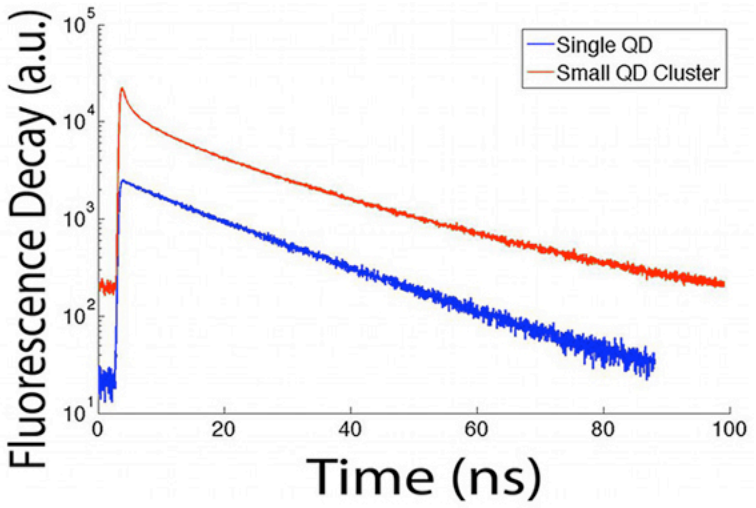

Figure 23: Photoluminscence Decay Histograms

Photoluminescence decay histograms for isolated QD and QD clusters shown in figures 20 and 21. The difference in rise-times is due to variations in the instrument response function, which are accounted for in the fitting routine.

	τ_R(ms)	A	τ_1(ns)	B	τ_2(ns)
isolated QD	272	493 ± 5	1.2 ± 0.2	2002 ± 50	19 ± 1
QD Cluster	80	13180 ± 500	2.3 ± 0.2	5074 ± 50	16 ± 1

Table 2: Summary of Fitting Parameters

Summary of fitting parameters extracted from eq 13 and 14 for the isolated QD (figure 20) and QD cluster (figure 21).

The results presented above suggest that QD clusters are characterized by unusually fast blinking and bi-exponential fluorescence decay dynamics. Figure 24 shows this relationship by plotting the fraction of the short-lived component $A/(A+B)$ of the fluorescence decay versus τ_R for 18 isolated QDs and 22 QD clusters, as determined by effective volume calculations[31]. We find two distinct groupings, the first with long τ_R and small contributions from the short-lived component, which correspond to isolated QDs, and the second with shorter τ_R and a larger contribution from the short-lived component, which corresponds to QD clusters. These groupings confirm that the behaviors shown in figures 20 , 21 and 23 are consistently observed for a large number of isolated QDs and QD clusters.

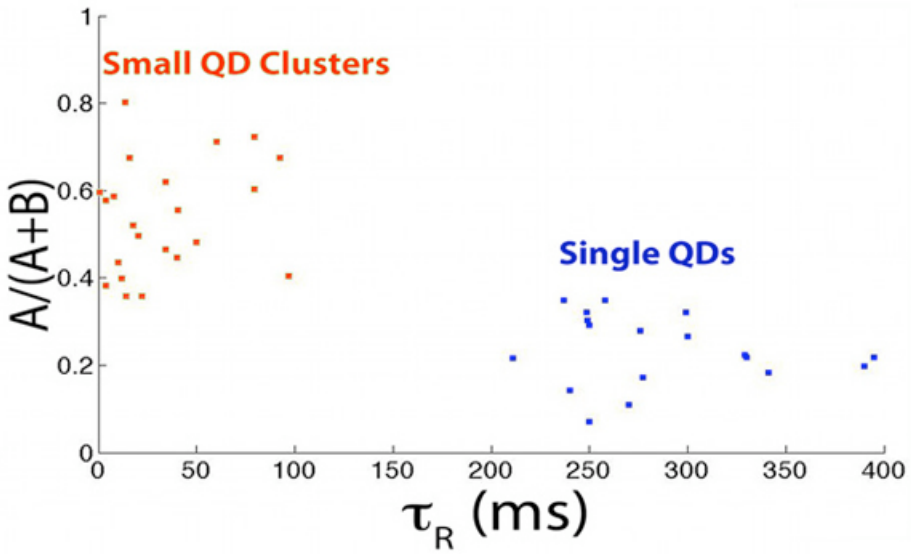

Figure 24: Fast Photoluminscence Decay vs Roll-OffTime

Fractional amplitude of the short-lived photoluminescence decay component versus roll-off lagtime, τ_R, for all studied particles.

Figures 25 and 26 present fluorescence lifetime-intensity distributions[126] (FLIDs) for the isolated QD and QD cluster presented in figures 20 and 21. To generate FLIDs, the photon data stream is parsed into 10 ms intervals, the fluorescence decay time is calculated from the photons detected within each interval, and plotted versus the number of detected photons within that interval.

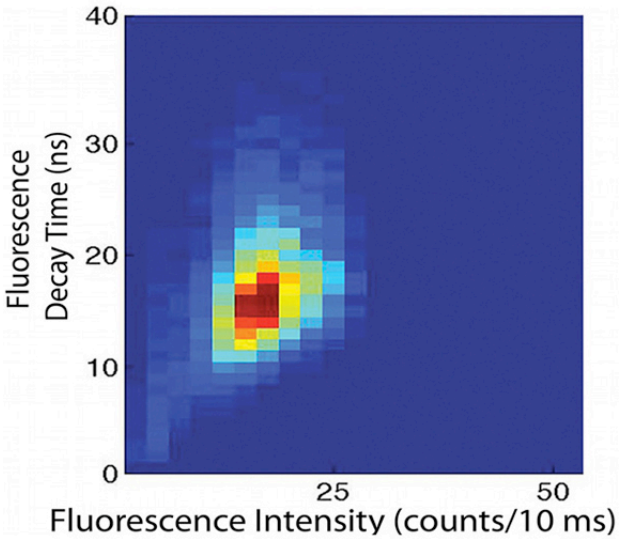

Figure 25: Isolated QD FLID

Fluorescence lifetime-intensity distribution (FLID) of the isolated QD from figure 20.

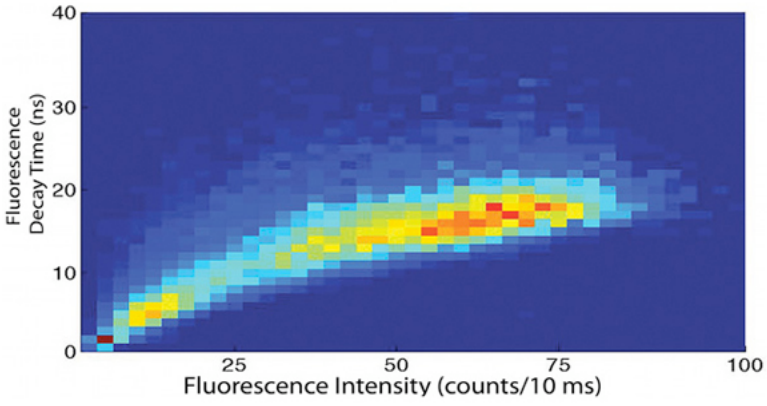

Figure 26: QD cluster FLID

Fluorescence lifetime-intensity distribution (FLID) of the QD cluster from figure 21.

The isolated QD shows one peak centered on the τ_2 listed in table 2, while the QD cluster has two distinct features, one located at τ_1, correlated with low fluorescence intensity and another located at τ_2, correlated with high fluorescence intensity. The observed correlation between low fluorescence intensity and fast fluorescence decay suggests that there exists rapid energy transfer between the closely packed QDs in the cluster. Such energy transfer has been observed in two-QD clusters that were engineered to have smaller QDs act as exciton donors to larger QDs[151]. In the present experiments, the variability of the QDs in the clusters is due to the limitations of colloidal synthesis, which gives at least a five percent size distribution in our stock QD solutions.

To understand how energy transfer can give rise the bi-exponential decay dynamics and observed intensity-lifetime correlations in QD clusters, we consider a simplified case of energy transfer involving two interacting QDs of slightly different energy gaps (figure 27). There are four possible *on* and *off* configurations for this system, which lead to two distinct levels of fluorescence intensity. In case I, both QDs are in the *off* state, resulting in no emitted photons. In case II, QD1 (the donor) is in the *on* state and QD2 (the acceptor) is in the *off* state, resulting in low intensity emission that occurs on a time scale faster than the energy transfer. In case III, QD1 is *off* and QD2 is *on*, leading to emission at the characteristic lifetime and intensity of QD2. In case IV, both QDs are in the *on* state, leading to possible emission at both the quenched lifetime and intensity of QD1 and the characteristic lifetime and intensity of QD2. In summary, cases I and II are responsible of the majority of low fluorescence intensity and/or rapid fluorescence decay, whereas case III and IV are responsible for the higher fluorescence intensity and slow fluorescence decay. Independent blinking of the individual QDs gives rise to fluctuations in the fluorescence intensity that is modulated by the energy transfer between QD1 and QD2. This simple model shows how coupling between QDs in a cluster may explain the phenomenon of enhanced

blinking.

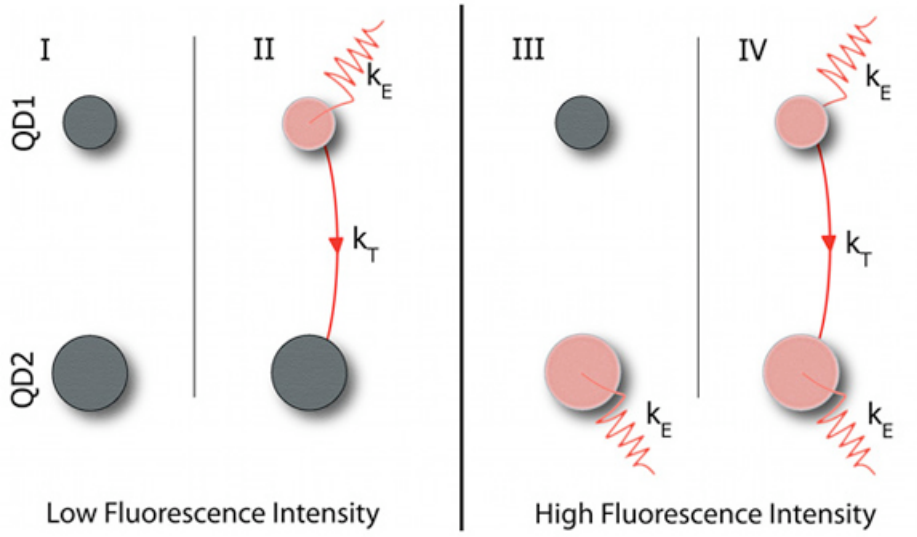

Figure 27: Possible Energy Pathways Between Two Coupled QDs
Proposed schematic for energy transfer kinetics of two closely packed QDs with different energy gaps. There are four cases to consider, depending the on (orange) or off (grey) state of each QD.

To extend this proposed energy transfer concept, we have created a detailed kinetic model for an arbitrary number N of interacting QDs based on the following assumptions:

1. We assume that each of the QDs in a cluster blinks independently, and that the statistical properties of the fluorescence intermittency for the individual QDs are unaffected by their proximity to other QDs. Experimental *on*/*off* distributions are used to create the time dependent *on*/*off* state of the individual QDs within a given cluster.

2. We assume the QDs all have slightly different energy gaps, and a relaxed exciton can move from one QD to another QD with smaller energy gap[2]. This is the crucial assumption of model. Note that no particular physical mechanism for the energy transfer is implied.

3. We assume that only one QD in a cluster is excited per pulse, and that the excitation quickly relaxes to the lowest energy exciton. We verified that this assumption holds well at average laser powers less than 2 μW. For the sake of simplicity, we have made the further assumption that all QDs have the same excitation cross-section.

4. An exciton in an *off* QD rapidly recombines through a non-radiative pathway[65, 152], whether excited directly by photon absorption or by nonradiative energy transfer from another QD in the cluster. This is consistent with the absence of a strong short lifetime feature in the fluorescence decay histograms for isolated QDs.

5. An exciton in an *on* QD either recombines radiatively or transfers to a smaller energy gap QD that may be *on* or *off* [65, 147, 152, 158, 159]. We assume that an exciton in an *on* QD can decay radiatively, at the rate k_E known from the fluorescence lifetime of isolated QDs, or that it can be transferred, at the rate k_T, to any of the QDs in the cluster with smaller energy gap. Nonradiative relaxation in *on* QDs is neglected. The rate of emission, k_E, is given by $\langle \tau_2^{-1} \rangle = 5 \times 10^8\,\mathrm{s}^{-1}$ and the rate of energy transfer is approximated as $k_T = 10k_E$ based on the observed ratio between τ_1 and τ_2 (Table 2).

These assumptions lead to a set of kinetic equations for the probability that a QD in the cluster is electronically excited; but note that the equations depend on the *on/off* state of the QDs in the cluster, referred to as the *on/off* configuration. Let us consider an example with $N = 4$ and suppose QD3 is *off* and the others are *on*.

This leads to the following set of differential equations, where p_i is the excitation probability and we label the QDs in order of increasing energy gap:

$$\begin{aligned} \tfrac{dp_4}{dt} &= -k_E p_4 - 3k_T p_4 \\ \tfrac{dp_2}{dt} &= -k_E p_2 - k_T p_2 + k_T p_4 \\ \tfrac{dp_1}{dt} &= -k_E p_1 + k_T p_2 + k_T p_4 \end{aligned} \tag{15}$$

Note the factor of three in the rate of loss by energy transfer from QD_4, because there are three QDs with smaller energy gaps. Taking $p_1 = p_2 = p_4 = 1$ as the initial conditions (we do not consider excitation of the dark QD), the fluorescence intensity is proportional to $S(t) = k_E(p_1 + p_2 + p_4)$. Note the extreme simplicity of the model, with only two dimensionless parameters, N and k_T/k_E.

To construct model fluorescence trajectories for a given a value of N we generate independent *on/off* trajectories for each of the QDs at 10 ms time resolution. The *on/off* state of the QDs determines the appropriate rate equations; there is a distinct set of equations for each of the 2^N configurations of the cluster. Each set of equations is analytically solved in advance using Maple to determine the time-dependent, initial-condition summed solution $S(t)$. The quantum yield

$$QY \equiv \frac{1}{N} \int_0^\infty S(t)dt \tag{16}$$

and average lifetime

$$\langle \tau \rangle = \int_0^\infty tS(t)dt \Big/ \int_0^\infty S(t)dt \tag{17}$$

within each time bin are thus determined. An excitation rate is chosen to reproduce the experimental average number of counts per bin for an isolated *on* QD and the value of the model fluorescence trajectory in each time bin is drawn from a Poisson distribution with the average value determined by the product of the quantum yield,

the single-QD excitation rate, and the number of QDs in the cluster. The Poisson statistics account for the probabilistic character of both the excitation process and the emitted photon collection. The ACF is then calculated using eq 13 for the resulting fluorescence trajectory.

By correlating fluorescence intensity with the calculated average lifetime, we can generate FLIDs. The lifetimes are broadened in accord with

$$P(\tau) = I^I \tau^{I-1} e^{-I\tau/\langle\tau\rangle} / \langle\tau\rangle^I (I-1)! \tag{18}$$

the probability distribution function for the average of I (the number of photons in a bin) identically distributed exponential random variables.

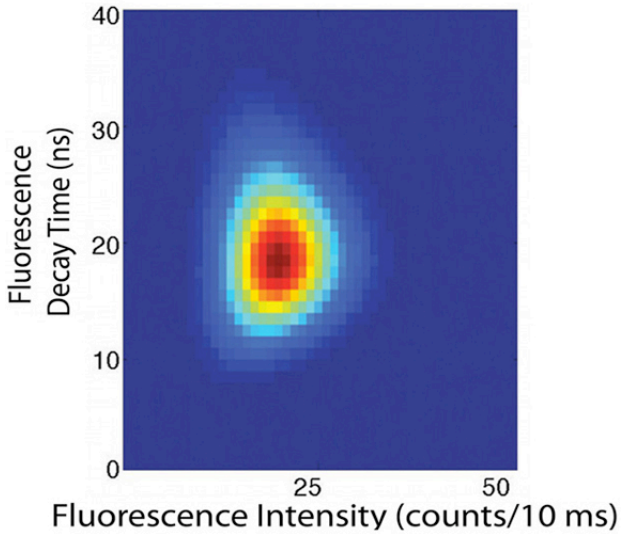

Figure 28: Simulated Single QD FLID
Simulated FLID for an isolated QD with $k_E = 5 \times 10^8 \mathrm{s}^{-1}$.

Figures 28 and 29 show the FLIDs generated from our model calculations for $N = 1$ and 4, which are generally consistent with the overall shape of the experimental FLIDs (figures 25 and 26). For the QD cluster, there is a broad intensity distribution corresponding to the longer lifetime component in both the model and experimental FLIDs. This occurs when the smallest energy gap QD is *on* and is responsible for the

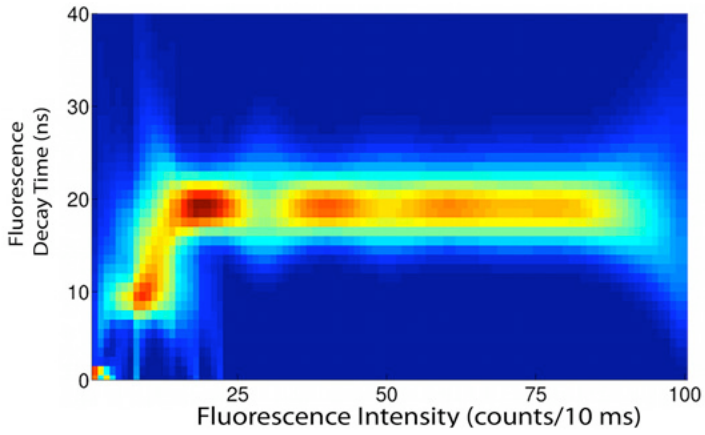

Figure 29: Simulated Cluster QD FLID
Simulated FLID for a 4 QD cluster with $k_E = 5 \times 10^8 \mathrm{s}^{-1}$ and $k_T = 5 \times 10^9 \mathrm{s}^{-1}$.

majority of the detected emission at fluorescence decay time τ_2. The broad intensity distribution is due to multiple possible *on*/*off* configurations of the remaining QDs. The maximum intensity occurs when all QDs are *on*; whereas, the lowest intensity within the feature at τ_2 occurs when only the smallest energy gap QD is *on*. When the smallest energy gap QD is *off*, energy transfer from the higher energy gap QDs results in partially quenched emission at the shorter fluorescence decay time τ_1. This accounts for the feature in the lower left corner of figure 29. Intermediate fluorescence decay times are also observed in the simulated FLIDs, due to energy transfer among the QDs with intermediate energy gaps.

Figures 30 and 31 display the simulated fluorescence trajectories and autocorrelation functions for QD clusters with $N = 1 - 4$. As more QDs are added to the cluster, the blinking becomes more rapid, while the 50% decay of the ACF occurs at shorter lagtime. This behavior is qualitatively similar to the experimental data presented in figures 21 and 22. According to our model, energy transfer to a QD with a smaller energy gap becomes more probable as the cluster size increases. Whenever a QD switches to an *off* state the emission is partially quenched. Consequently, fluctuations in intensity within the high intensity state are more frequent with increasing

N. Off QDs act as energy sinks for the entire cluster, with the QD of smallest energy gap playing a special role in determining whether the cluster is in a state of high of low fluorescence intensity. These results explain the unique photo-physical properties of QD clusters described in both this work and our previous study, namely the faster blinking and ACF decays of QD clusters vs. isolated QDs[31, 133]. The alternate explanation originally presented by our group and recently expanded upon by Lee and Maenosono cannot account for processes occurring on faster timescales than the radiative rate of the QDs, which is the key observation of the present work[31, 155].

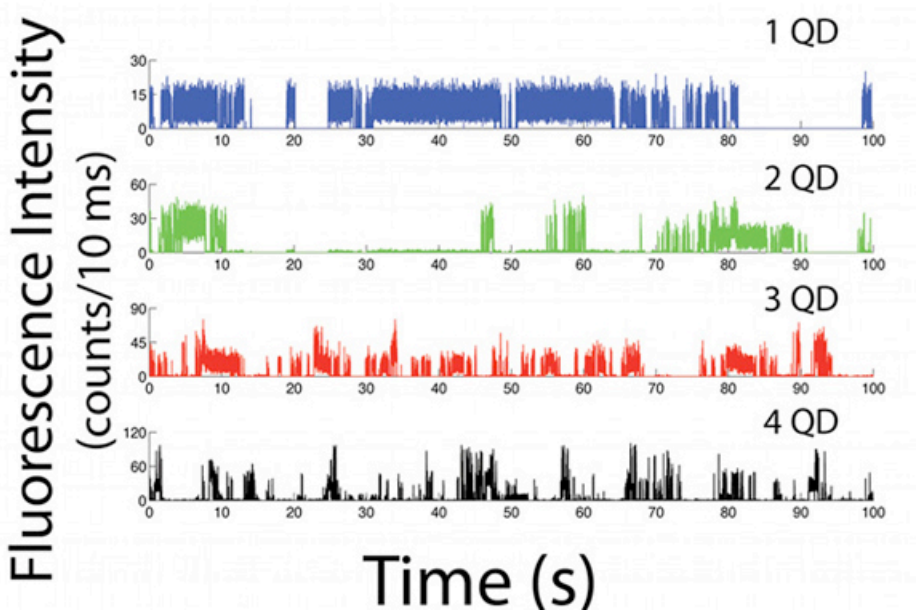

Figure 30: Simulated Fluorescence Trajectories
Evolution of the fluorescence trajectory as more QDs are added to the cluster.

Because these calculations are based on single *on*/*off* configurations in every time bin, we have not accounted for *on*/*off* transitions in the middle of those intervals. Thus the existence of only 2^N values for the average intensity and lifetime is an artifact of the binned calculations, and a continuous-time calculation would lead to broadening of the distinct features seen in the model FLIDs such as figures 28 and 29. However, we do not expect that the systematic variation of ACF with N seen in figure 31, which is associated with time scales much greater than a single bin, would

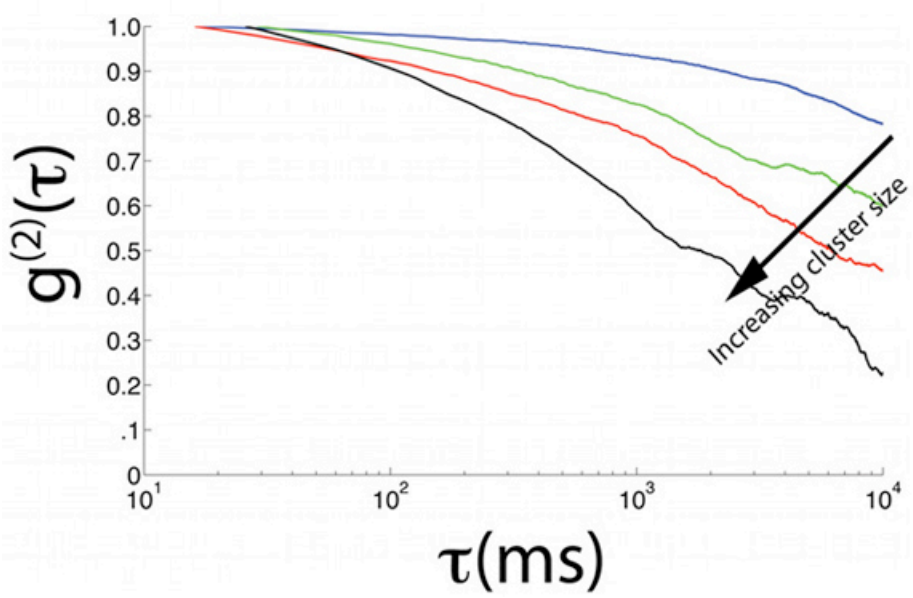

Figure 31: Autocorrelation Functions of Simulated Trajectories
Corresponding autocorrelation functions from figure 30, normalized at $\tau = 10$ms.

be significantly different in a continuous-time calculation.

Additionally, the assumption of independent blinking for the individual QDs might well be questioned. Previous work by Lee and Maenosono shows photo brightening in QD aggregates[155], suggesting a cooperative mechanism that suppresses transitions to *off* states. Recent work by the Drndic group that correlates blinking statistics of both individual and clusters of nanorods with TEM images suggests a cooperative blinking mechanism as well[141]. Such cooperation would not qualitatively affect the theoretical FLIDs, but would have difficult-to-predict effects on the quantitative results of both the ACFs and FLIDs obtained from the model.

Finally, let us discuss two possible mechanisms for energy transfer, FRET and Dexter exchange. We must reiterate that the current work cannot make strong claims about the mechanism, as we are unable to measure inter-QD distances. Curutchet *et al.* performed detailed calculations of self-FRET for CdSe nanocrystals and found that the electronic coupling drops to almost zero at inter-QD distances of greater than 7 nm[150]. The ligands on the QDs used in this work are 2 nm long, so the maximum

plausible nearest-neighbor (center-to-center) distance is roughly 7 nm. It is more likely that the ligands are intertwined, leading to smaller inter-QD distances well within the FRET range calculated by Curutchet *et al.* One must also consider Dexter exchange as a possibility, because the relevant electronic wave functions do extend outside the nanocrystals. However, it is difficult to estimate the rate of Dexter exchange between colloidal QDs because of the lack of theoretical work and experimental data.

4.4 Conclusion

The new experimental observations presented above, combined with our model simulations, provide a new perspective on how inter-QD coupling in the context of *on*/*off* blinking can alter the photo-physical properties of even small numbers of coupled QDs. The primary contribution of this work is the observation that during periods of low fluorescence intensity, closely packed QDs in a cluster exhibit fluorescence emission on a time scale that is intermediate between the natural lifetime of an isolated QD in its *on* state, and the non-radiative recombination time of an *off* QD. We attribute this intermediate timescale to energy transfer from larger energy gap QDs to smaller energy gap QDs. We have also demonstrated that the proposed mechanism, implemented in a minimal model, accounts for all of our observed experimental results in QD clusters. This confirms that the information obtained from single-molecule spectroscopic studies can be utilized to investigate the electronic interactions of QDs in higher order structures.

Some consequences of the model depend on the assumed value of N, the number of QDs in the cluster, such as the autocorrelation function and the intensity distribution of the long lifetime component. Thus an important element of future work should be the control or measurement of N, which will enable further validation and refinements to the energy transfer model. Additional experiments in which the distances between QDs in a cluster are chemically manipulated or measured combined with resolution

of the fluorescence into separate spectroscopic components are necessary in order to gain insight into the physical mechanism underlying the energy transfer between similar sized, closely packed QDs. In our group, Kevin Whitcomb has pursued this by depositing QDs onto a SiN TEM grid (obtained from the Drndic group) and attempting correlate the TCSPC data with TEM images by etching markers into the TEM grid, but so far has been unsuccesful. The Hwang group has succesfully used a modified mass-spectrometer to separate charged NC clusters and are able to correlate cluster size from $N = 1 - 4$ to fluorescence trajectories[133]. Their measurements confirm the unique properties of small NC cluster fluorescence trajectories, but do not use pulsed excitation and as such do not measure photoluminescence decay.

Another open question is how exactly this emergent behavior will effect device performance. At best, devices that extract energy from the QDs on timescales faster than electronic energy transfer occurs will be unaffected. However, devices that rely on longer timescale processes, such as solar cells that involve diffusive exciton transport (see, for example, the recent discussion of QD-based photovoltaic devices by Pattantyus-Abraham, *et al.* [15]), will be subject to energy loss whenever QDs acting as energy sinks are in the *off* state. Further study of these devices on the single-molecule level is necessary to fully understand the implications of this work.

4.5 Supporting Information: Sample Preparation

The method for obtaining clusters of QDs out of solution was outlined in section 4.2. We would like to briefly expand here on both the choice of QDs and mica surface functionalization with ATPES. The original experiments performed by Dr. Ming Chen showed interaction between core-shell QDs synthesized by Evident Technologies. A change in synthetic procedures by Evident to improve the resistance of their QDs to physical degradation, essentially enlarging the shell layer, eliminated any coupling between adjacent QDs and therefore the effects seen by Dr. Chen. Throughout the

work presented here, we have utilized core-shell QDs synthesized by Ocean Nanotech, with a nominally 2 monolayer thick ZnS shell. These QDs have slightly higher QYs and fractional on times than the Evident Technologies QDs but the same emission wavelength and similar absorption spectra.

To prepare a surface suitable for both optical and AFM measurements, we start with mica chips. Thin mica chips are obtained by peeling layers of mica off of the chip with a razor blade. A small drop of optical glue is placed on a coverslip, which is then slightly heated and the mica chip placed on top of the glue. By heating the glue, we lower the viscosity and create a thin, uniform layer underneath the mica chip. The coverslip is then placed under a UV lamp for 25 minutes to cure the optical glue. A fresh mica surface is prepared by taking a piece of scotch tape, placing it onto the mica chip, and peeling it off along with the top layer of mica. This surface is suitable for optical measurements, but we have found that the AFM tip will drag NCs along the surface. To finish preparing the surface for our experiments we functionalize the mica surface with 30 μL of ATPES in a vacuum chamber for 15 minutes. This surface coating immobilizes the NCs through electrostatic interactions with the TOP/TOPO ligands without affecting the photophysical properties of the NCs.

Core-shell QDs from Ocean Nanotech are suspended in toluene, which we take advantage of to create the NC clusters. First we dilute the NCs to an appropriate concentration for SMS measurements, typically 1:1000 in optical quality toluene. Then, 5-15μL of anhydrous methanol is introduced into the diluted solution and let sit for approximately 15 minutes. A 40-100 μL aliquot, depending on the size of the mica chip, is spin coated at 4000 RPM onto the chip. This preparation reliably provides a mix of isolated individual NCs and small NC clusters, biased towards to the NC clusters.

4.6 Supporting Information: Modeling Individual NC And NC Cluster Fluorescence Trajectories

Here we expand on the assumptions made in our simulation of the fluorescence trajectories and FLIDs for clusters of size $N = 1$ to $N = 4$. Starting with our assumption of independent blinking of the individual NCs. To create fluorescence trajectories for individual NCs, we begin with the idea that both the on and off time probability distributions follow an inverse power-law,

$$P(t) = At^m \tag{19}$$

with m varying slightly between our experimentally obtained on and offdistributions, $m_{on} = -1.5$ and $m_{off} = -1.7$. To create sample fluorescence trajectories for individual NCs, we begin by defining a cutofftime, t_0, that allows us to normalize the probability distribution. Given a paticular t_0 and m, we have the normalization constant,

$$A = -\frac{m+1}{t_0^{m+1}} \tag{20}$$

and construct the comulative probability distribution,

$$C(t) = \int_{t_0}^{t} P(t')dt' = 1 - (\frac{t_0}{t})^{m+1} \tag{21}$$

and invert equation 21 to obtain

$$t = t_0(1 - C(t))^{\frac{-1}{m+1}} \tag{22}$$

from which we uniformly sample $C(t)$ between 0 and 1 to generate the time that a NC spends a given state. We typically create 100-300 second fluorescence trajectory for each NC at 1 millisecond time steps, mainly due to memory limitations on our

computers. An example table of the first ten random numbers, time, and state for a given individual NC is shown in table 3. Once a full fluorescence trajectory is generated, the on state is set to the experimentally determined intensity for a given bin size. The whole fluorescence trajectory is then broadened according to Poisson statistics. This leaves us with a completed individual NC fluorescence trajectory, shown in figure 32.

C	t	state
.09	1200	on
.54	65	off
.95	37	on
.96	29	off
.16	585	on
.49	78	off
.80	48	on
.14	457	off
.42	129	on

Table 3: Individual QD Blinking Simulation Time Periods
Example of first ten time periods of individual NC trajectory generated from power law statistics.

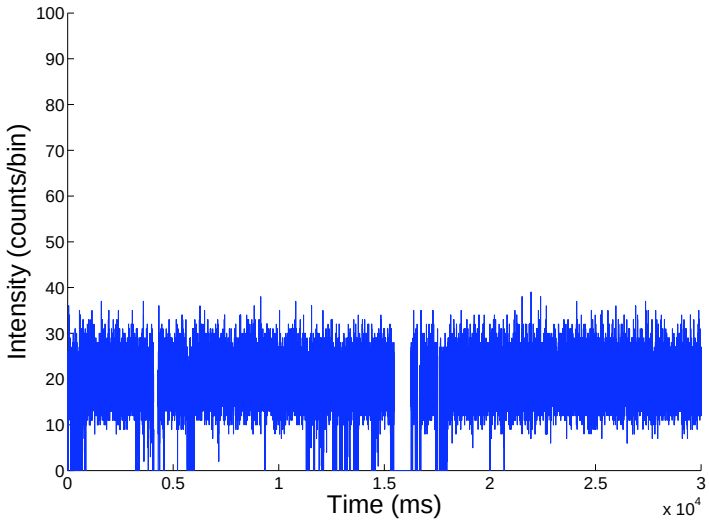

Figure 32: Simulated Fluorescence Trajectory for Individual NC
Simulated fluorescence trajectory for a single quantum dot from power-law statistics.

To generate the fluorescence trajector for a QD cluster, we follow the above procedure for N QDs, but do not broaden the trajectory at first. Once N individual fluorescence trajectories are generated, we proceed to evaluate the N trajectories bin-by-bin to determine the state of the cluster. Our second assumption is that there exists a pathway for energy transfer between QDs within the cluster [35, 65, 147, 150, 152]and that there exists a size dispersion within a batch of QDs lead us to believe that the master equation proposed in eq 15 is a reasonable approximation for the excited state of the cluster. We assume that we can encompass the multiple possible energy transfer and non-radiative recombination pathways with a single rate constant, k_T. We precalculate all 2^N variations of eq 15 to determine the quantum yield and lifetime for each possible state of the cluster. These are summarized below in table 4. The final cluster fluoresence trajectory is then broadened according to Poisson statistics. For the data generated in figures 28, 29, 30, and 31, we assume there is no possibility of energy transfer from a NC of smaller bandgap to a NC of larger bandgap, which we will refer to as "back transfer". We will discuss the ramifications of this assumptions and how allowing for back transfer affects the model in the following section.

N	Configuration	QY	τ_{avg}
1	0	0	0
	1	1	1
2	0, 0	0	0
	0, 1	0.05	0.09
	1, 0	0.5	1.0
	1, 1	1.0	1.0
3	0, 0, 0	0	0
	0, 0, 1	0.02	.05
	0, 1, 0	0.03	.09
	1, 0, 0	0.33	1.0
	0, 1, 1	0.06	.09
	1, 0, 1	0.51	0.98
	1, 1, 0	0.66	1.0
	1, 1, 1	1.0	1.0
4	0, 0, 0, 0	0.0	0.0
	0, 0, 0, 1	0.01	0.03
	0, 0, 1, 0	0.01	0.05
	0, 1, 0, 0	0.02	0.09
	1, 0, 0, 0	0.25	1.0
	0, 0, 1, 1	0.02	0.05
	0, 1, 0, 1	0.04	0.09
	1, 0, 0, 1	0.33	0.98
	0, 1, 1, 0	0.05	0.09
	1, 0, 1, 0	0.38	0.98
	1, 1, 0, 0	0.5	1.0
	0, 1, 1, 1	0.07	0.09
	1, 0, 1, 1	0.51	0.97
	1, 1, 0, 1	0.67	0.99
	1, 1, 1, 0	0.75	1.0
	1, 1, 1, 1	1.0	1.0

Table 4: Four QD Cluster Lifetimes and Quantum Yields with Zero Back Transfer Results of solving equation 13 for N=1,2,3,4. For the configuration, 0 is a NC in the off state and 1 is a NC in the on state. Here we assume there is no possibility of back energy transfer. QY and τ_{avg} are given as mutliples of the experimentally maximum possible determined values.

4.7 Supporting Information: Generating Theoretical Fluorescence Lifetime Intensity Distributions

To generate FLIDs from the experimental fluorescence trajectories, the lifetime in each 10 ms bin is calculated and plotted versus the total photon intensity in that bin. Because we are not simulating the response of the NCs to the laser pulse, but rather creating fluorescence trajectories based on experimental *on/off* distributions, we cannot exactly replicate the experimental process but rely on our calculated quantum yields and lifetimes given in table 4. To generate FLIDs we first create Poisson distributions for each possible state of the cluster centered around the quantum yield for that state multiplied by the experimentally determined "bright" state for the cluster. We then broadened the distribution along the lifetime axis by applying eq 18, weight each 2D distribution according to the percentage that an individual cluster spends in those states according to the generated fluorescence trajectory, and add all them all together. The results of this are shown in figures 28 and 29.

An important issue to consider is the possibility of back energy transfer. For all of the work so far, we have assumed a uni-directional flow of energy in the system. If we allow for one back energy transfer at the rate k_{BT}, it modifies equation 15 to give the following,

$$\begin{aligned} \frac{dp_4}{dt} &= -k_E p_4 - 3k_T p_4 + k_{BT}(p_2 + p_1) \\ \frac{dp_2}{dt} &= -k_E p_2 - k_T p_2 - k_{BT} p_2 + k_T p_4 + k_{BT} p_1 \\ \frac{dp_1}{dt} &= -k_E p_1 - 2k_{BT} p_1 + k_T p_2 + k_T p_4 \end{aligned} \tag{23}$$

and has important ramifications for the end-shape of the FLIDs. Shown in figure 33 are three FLIDs where the ratio of k_{BT}/k_T is varied from 0.1 to 1. None of these predicts the correct features of the experimentally obtained FLIDs, strongly supporting our original assumption of negligible back transfer. At the end of this section in table 5, we have listed the tabulated quantum yields and lifetimes for the three cases.

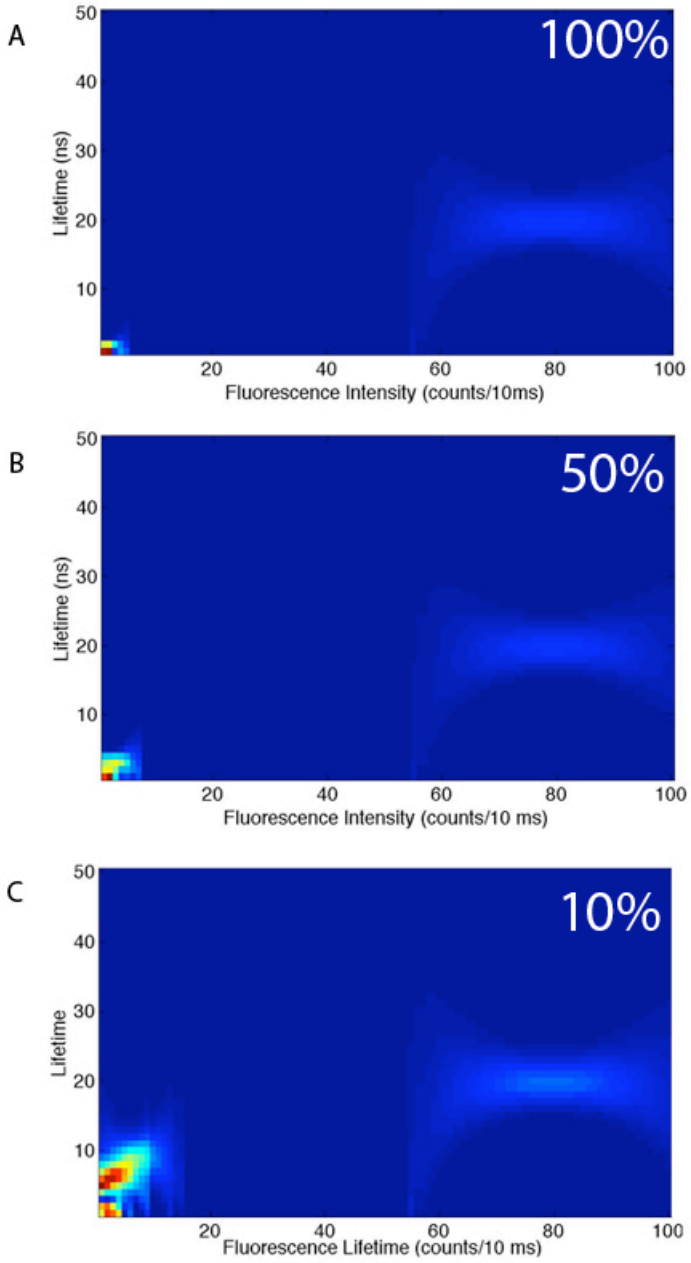

Figure 33: Bi-Directional Energy Transfer FLIDs

Results of allowing one back energy transfer per excitation. The percentage values given are in relationship to the forward transfer rate, i.e. for (A) $k_{BT}/k_E = 1$, (B) $k_{BT}/k_T = 0.5$, and (C) $k_{BT}/k_T = 0.1$. The obvious change in behavior from figure 26 verifies that the while complete uni-directional energy transfer is thermodynamically impossible, we do have a forward biased system where the rate of back energy transfer is less than 10 percent.

		$k_{BT}/k_T = 1$		$k/k_T = .5$		$k_{BT}/k_T = .1$	
N	Configuration	QY	τ_{avg}	QY	τ_{avg}	QY	τ_{avg}
1	0	0	0	0	0	0	0
	1	1	1	1	1	1	1
2	0, 0	0	0	0	0	0	0
	0, 1	0.05	0.09	0.05	0.09	0.05	0.09
	1, 0	0.05	0.09	0.08	0.16	0.25	0.5
	1, 1	1.0	1.0	1.0	1.0	1.0	1.0
3	0, 0, 0	0	0	0	0	0	0
	0, 0, 1	0.02	0.05	0.02	0.05	0.02	0.05
	0, 1, 0	0.02	0.05	0.02	0.06	0.03	0.08
	1, 0, 0	0.02	0.05	0.03	0.09	0.11	0.33
	0, 1, 1	0.06	.09	0.06	0.09	0.06	.09
	1, 0, 1	0.06	0.09	0.09	0.13	0.22	0.40
	1, 1, 0	0.06	0.09	0.11	0.17	0.33	0.5
	1, 1, 1	1.0	1.0	1.0	1.0	1.0	1.0
4	0, 0, 0, 0	0.0	0.0	0.0	0.0	0.0	0.0
	0, 0, 0, 1	0.01	0.03	0.01	0.03	0.01	0.03
	0, 0, 1, 0	0.01	0.03	0.01	0.04	0.01	0.05
	0, 1, 0, 0	0.01	0.03	0.01	0.05	0.02	0.08
	1, 0, 0, 0	0.01	0.03	0.02	0.06	0.06	0.25
	0, 0, 1, 1	0.02	0.05	0.02	0.05	0.02	0.05
	0, 1, 0, 1	0.02	0.05	0.03	0.06	0.04	0.08
	1, 0, 0, 1	0.02	0.05	0.03	0.07	0.10	0.26
	0, 1, 1, 0	0.02	0.05	0.03	0.06	0.04	0.08
	1, 0, 1, 0	0.02	0.05	0.04	0.08	0.12	0.28
	1, 1, 0, 0	0.02	0.05	0.05	0.09	0.17	0.33
	0, 1, 1, 1	0.07	0.09	0.07	0.09	0.07	0.09
	1, 0, 1, 1	0.07	0.09	0.09	0.12	0.20	0.33
	1, 1, 0, 1	0.07	0.09	0.11	0.14	0.30	0.43
	1, 1, 1, 0	0.07	0.09	0.13	0.17	0.38	0.5
	1, 1, 1, 1	1.0	1.0	1.0	1.0	1.0	1.0

Table 5: Four QD Cluster Lifetimes and Quantum Yields With Varying Amounts of Back Transfer
Results of solving eq 23 for three values of k_{BT}/k_T for $N = 1, 2, 3, 4$. For the configuration, 0 is a NC in the off state and 1 is a NC in the on state. QY and τ_{avg} are given as mutliples of the experimentally maximum possible determined values.

4.8 Supporting Information: Analysis of Fluorescence Lifetime Intensity Distribution

The information contained used to construct the FLIDs are "good" photon-laser pulse pairs, which means that dark counts and the rare multiple photon events per pulse are discarded when the FLID is constructed. By projecting onto the the x (intensity) or y (lifetime) axis, it is possible to re-construct the "true lifetime distribution" or "true photon counting histogram" (TPCH). We have compiled the TPCH for all of the data points shown in figure 24, excluding a few in the process because of issues with the Picoquant fitting routines. An example TPCH is shown in figure 34 where we note a few key features. For QD clusters, the low intensity state is consistently centered around 10 counts per 10 ms bin with a valley between the low intensity peak and higher intensity peak. Both the height and width of the high intensity peak varies significantly between individual clusters. In a attempt to establish a trend in TPCHs between all QD clusters, we integrate the area underneath both the low intensity and high intensity peaks and then take the ratio. The average ratio for "cluster like" FLIDs is .0350 with a standard deviation of .0172. Unfortunately, because we lack spatial information on the number N of QDs within each cluster, we cannot calibrate the width of the high intensity TPCH peak to N. Further experiments that resolve N within a cluster will provide this information and allow for a more detailed analysis of how the TPCH varies with N. The supporting information contains all FLIDs and their corresponding TPCH plots.

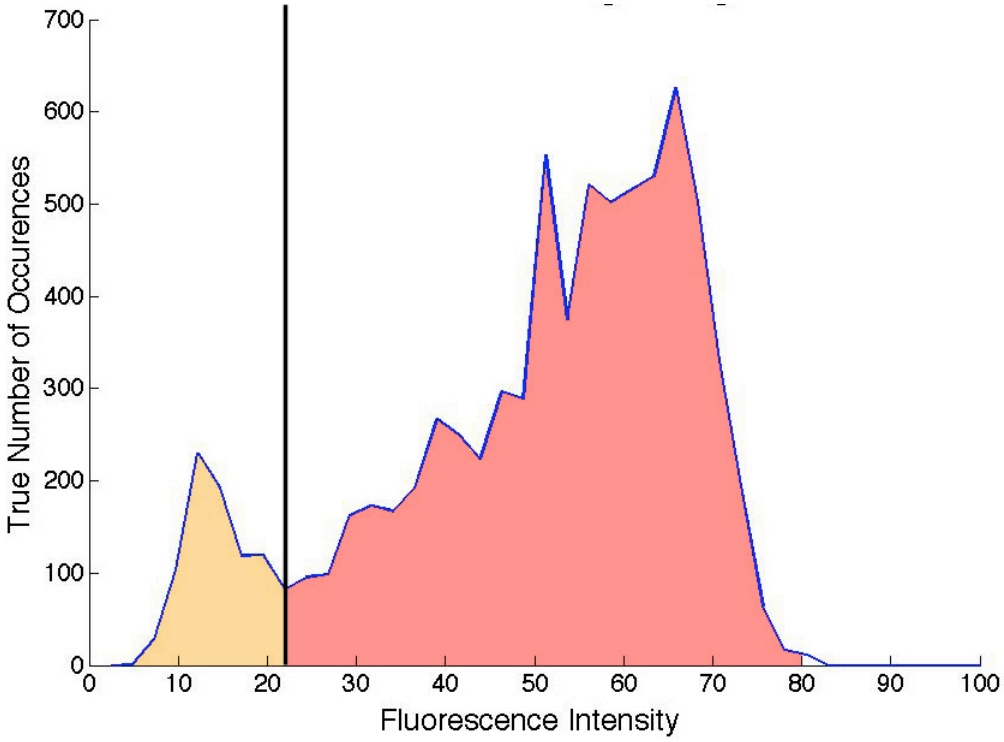

Figure 34: True Photon Counting Histogram of a QD Cluster
True Photon Counting Histogram (TPCH) calculated from fluorescence intensity lifetime distribution of a individual QD cluster.

5 Quantum Dot Sensitized Solar Cells

The work in this chapter is a collaboration between Justin Sambur and Yong-Qi Liang in the Parkinson group and myself. It is currently in submission for publication. Justin and Yong-Qi performed the QD synthesis and photoelectrochemical measurements. Yong-Qi prepared the ZnO samples, Justin and I prepared the TiO_2 substrates. I took all the photoluminescence data, designed and constructed the sample chamber, analyzed the data, and conceived of the experiment. I am the lead author on the publication, with major contributions from Justin.

5.1 Overview

In Chapter 4 we proposed that QDs in close proximity interact and create "energy sinks", where an electron-hole pair created by an absorbed photon may be transfered to a QD in the *off* state and undergo non-radiative recombination on a timescale that is at most a few nanoseconds. This has obvious implications in QD based devices, particular photovoltaic devices, where electron-hole pairs must survive long enough to be separated and then harvested. Can we address this question utilizing our "bottom-up" approach? Thin film based devices present challenges to single molecule spectroscopy because it is impossible to isolate individual QDs or small QD clusters in the confocal region. An alternative configuration to thin film based devices are single crystal QD sensitized solar cells that rely on sub-monolayer surface coverage of QDs on either single cystal TiO_2 or ZnO.

Due to the size and material dependent band gaps[1, 2, 16], relative ease of ligand exchange[45, 160] and possibility of multiple exciton generation[57, 101] QDs are

actively explored as the light-harvesting layer in thin films[15, 75, 97, 161–163], hybrid QD-polymer solar cells[90, 92, 164–166] and QD-sensitized solar cells (QDSSCs)[89, 94, 96, 153, 156, 167–171]. Regardless of the device architecture, overall efficiency partly depends on separation of photo-excited electron-hole pairs and collection of carriers at their respective contacts on a time scale faster than radiative or non-radiative recombination pathways[29, 102–112].

Optical measurements that probe the lifetime and bleach of the QD excited state, such as time resolved photoluminescence (trPL) and transient absorption (TA), have been extensively used to determine electron transfer rates in QDSSCs by comparing optical signatures of QDs in solution or QDs adsorbed on an insulating surface to QDs adsorbed on mesoporous metal oxide supports[109]. Studies have shown that there is a quenching of the PL intensity and radiative lifetime of the QDs once coupled to the electron acceptor, but very few of these experiments have attempted to measure the photocurrent-response on the same system. Bonn and co-workers recently utilized trPL, TA, terahertz spectroscopy (THz-S), and photocurrent-voltage behavior to study electron injection from the lowest excited states of PbSe QDs to mesoporous TiO_2 or SnO_2 nanoparticle films[110]. By varying the energetics of the electron acceptor (TiO_2 or SnO_2 nanoparticles), Pijpers *et al.* were able to confirm electron injection only occurs when energetically possible (the SnO_2 system) via THz-S and photocurrent measurements but that solely characterizing the system via optical methods indicates electron injection in both systems (SnO_2 and TiO_2). Although ultrafast optical experiments may provide useful information regarding the time scale of electron injection, these methods do not measure current in an external circuit. Since the absorption and photoluminescence characteristics of QDs are critically dependent on surface chemical treatments[172], interpretation of changes in optical properties may be complicated by the surrounding medium (*e.g.* colloidal QDs, QDs adsorbed on insulators or QDs adsorbed on metal oxides).

We have utilized a model system consisting of dispersed CdSe QDs on single crystal semiconducting substrates, TiO2 and ZnO, at submonolayer coverages[100]. By varying the capping ligands, we focus exclusively on the effect of ligand chemistry on both sensitized photocurrent yields and quenching of the PL lifetime of the QDs, whose lowest excited states have sufficient energy to inject electrons into the conduction bands of TiO2 and ZnO.

5.2 Experimental Setup

The QDs examined in this study consisted of CdSe core QDs capped with one of four ligands: trioctylphosphine oxide (TOPO), oleic acid (OA), 11-mercaptoundecanoic acid (MUA), and 3-mercaptopropionic acid (MPA). OA-capped QDs were synthesized via a hot-injection method. TOPO-capped QDs were purchased as a solid powder from Ocean Nanotech (QCO-600-0050, Springdale, Arkansas). The excitonic peak absorption maxima occured at 526 nm and 578 nm for the synthesized and Ocean Nanotech QDs (ON-QDs) respectively, corresponding to average core diameters of 2.8 nm and 3.8 nm[44, 56].

Synthesis of OA-capped QDs CdSe QDs were synthesized via the hot-injection method[44]. Typically, 0.256 g CdO (2.0 mmol, 99.998 %, Alfa-Aesar) was dissolved in 1.6 ml oleic acid (OA, 5.0 mmol, 90%, Alfa-Aesar) and 8.0 ml 1-octadecene (90%, Acros) and heated to 165°C under a N2 atmosphere to form a clear solution. A solution of 0.156 g Se (2.0 mmol, 99.999%, Alfa-Aesar) dissolved in 0.922 g Tri-n-octylphosphine (2.5 mmol, TOP, 90%, Alfa-Aesar) and 4.0 ml 1-octadecene was injected at 195°C. Growth at 180°C for various time intervals (1 min to 8 min) generates the QDs of desired size. The reaction was quenched via the injection of 10 ml toluene.

Ligand exchange of OA-capped QDs. Short (MPA) and long (MUA) bifunctional linker molecules were used to replace the OA ligands on the CdSe QDs.

Typically, the CdSe QDs in 0.8 ml toluene (OD ≈70) were precipitated with ethanol (absolute purity, Pharmco-Aaper). Then the precipitated solid was transferred to 60 ml methanol (99.9%, Fisher scientific) in a 3-neck flask, followed by the addition of 0.080 g MUA (0.4 mmol), or 80 ul MPA (0.9 mmol) and 1.0 g tetramethyl ammonium hydroxide pentahydrate (TMAH, 5.5 mmol, 98%, Alfa-Aesar). The solution of CdSe QDs was refluxed for >6h under an N2 atmosphere. The final clear solution was precipitated with excess ethyl acetate (99.98%, EMD), and the precipitate was separated by centrifugation. MPA or MUA capped QDs were dissolved in ethanol and diluted to suitable concentration (whereby the optical density at the 1s transition was 0.2) for sensitization of TiO_2 or ZnO.

Ligand exchange of TOPO-QDs. We followed an adapted procedure developed by Peng and co-workers for CdSe core QDs[45, 160]. Briefly, 40 μl of MPA was added to 15 ml of methanol and adjusted to pH 11 with tetraethylammonium hydroxide. After degassing the solution for 30 min with high purity nitrogen, approximately 50 mg of CdSe QD powder was added and refluxed for 12 hr at 80°C. Following the ligand exchange procedure, the solution was centrifuged at 3000 rpm, and the supernatant was decanted. The methanol solution of MPA-capped CdSe QDs was stored in the dark under ambient conditions and was stable to aggregation for more than one year.

Preparation of TiO_2 single crystals. One-side mechanically polished crystals (10 mm x 10 mm x 1 mm) of rutile (110) were obtained from MTI Crystal Corporation (Richmond, CA). The as-received crystals were polished using 20 nm colloidal silica solution on Buehler polishing pads and annealed in air at 750°C for 6 hours[100]. The crystals were reductively doped by annealing for 30 min at 650°C in a 30:10 sccm stream of N2:H2. Following the reduction step, the crystals were re-polished with colloidal silica and annealed in N2 for 3 hr in an N2 atmosphere. The crystals were polished and annealed in N2 up to five times until the AFM images of the TiO_2

crystals exhibited a terraced surface structure. The crystals were mounted on copper disks with Ga/In eutectic to ensure an ohmic contact. A copper wire was soldered to the back of the disk and fed through a glass rod, at which point the entire electrode was sealed with epoxy (Epotek 377) and silicone rubber (RTV) and allowed to dry for a few hours.

Preparation of ZnO crystals. ZnO single crystals (0001, 10 mm x 10 mm x 1 mm) were purchased from MTI Inc. The samples were cleaned by ultrasonication in ethanol followed by immersion in 3.0 M NaOH solution for 5 minutes.

Sensitization of the single crystal electrodes. Bare crystals for AFM and photocurrent measurements were characterized via AFM prior to QD adsorption. Epoxy-mounted and unmounted TiO_2 crystals were immersed for 1 hr in methanol solutions of MPA ON-QDs and ethanol solutions of MUA-QDs. 5 μL aliquots of TOPO-QDs dissolved in toluene were pipetted on the crystal surface continuously for 20 min to avoid epoxy degradation from the organic solvent. The electrodes were rinsed with the same solvent used for QD adsorption and dried immediately with a 15 psi stream of N_2.

Photoelectrochemical measurements. Photoelectrochemical measurements were performed at short circuit in an aqueous sulfide electrolyte using a two-electrode configuration with a platinum wire counter electrode. Incident photon to current efficiency (IPCE) spectra, which measure the ratio of electrons collected to incident photons at discrete wavelengths of light over a given range, were obtained using a Stanford Research Systems (SRS) model SR570 low noise current preamplifier connected between the working and counter electrodes. The signal from the pre-amplifier was then fed into a SRS model SR830 DSP lock-in amplifier. Illumination from a 100 W Oriel lamp (385 nm cut-off filter) was passed through a computer controlled grating monochromator (2 nm step interval) and chopped at 13 Hz to provide a modulated photocurrent signal.

The raw photocurrent signal was corrected for photon flux using a lamp power spectrum recorded at 2 nm intervals using a themopile detector.

AFM Measurements. Tapping mode AFM (Digital Instruments Nanoscope IIIA controller and a multimode SPM) was used to characterize the CdSe QDs using an Olympus AC160TS probe with a 42 N/m force constant and resonant frequency of ≈300 kHz. AFM images were processed using Digital Instruments software.

Photoluminescence Decay Measurements. As shown in figure 35 a sample chamber consisting of a 75 μm optical glass coverslip on the bottom with plastic sides and top was constructed. The top of the chamber was drilled with two holes to allow for the electrode and counter-electrode wires to protrude. The sample chamber was mounted on the stage of an inverted optical microscope (Zeiss Axiovert S100) equipped with a piezoelectric scanner (Nanonics NIS-30 SC-100/28) for positioning in the optical probe region of the microscope. Excitation was provided by a 440-nm pulsed diode laser (PicoQuant LDH-P-C 440) operating at a pulse repetition rate of 10 MHz and pulse width of ≈100 picoseconds. The laser light was focused onto the stage using a 0.85 NA/60× microscope objective to form an approximately 1.0-μm-diameter optical probe region at the bottom surface of the semiconductor. An average power of approximately 350 nW was used to give a time-averaged excitation intensity of approximately 20 W/cm^2. Emitted fluorescence was collected by the same microscope objective and directed onto a single-photon counting avalanche photodiode detector (APD) (Perkin Elmer SPCM-14AQR). The emission was spatially filtered using a 50-μm diameter pinhole located in the image plane of the microscope and spectrally filtered using a 510 nm longpass filter before reaching the detector. The output of the APD was directed to a time-correlated single-photon counting module (PicoQuant TimeHarp 200) to record the photon data. The photon data was post-processed using vendor-supplied software (Picoquant SymPhoTime) to obtain photoluminescence intensity trajectories and decay histograms for each area. The

photoluminescence trajectories and decay histograms were obtained in four different working regimes:

1. Unmounted crystals
2. Mounted crystals
3. Mounted crystals with electrolyte
4. Mounted crystals with electrolyte at short-circuit

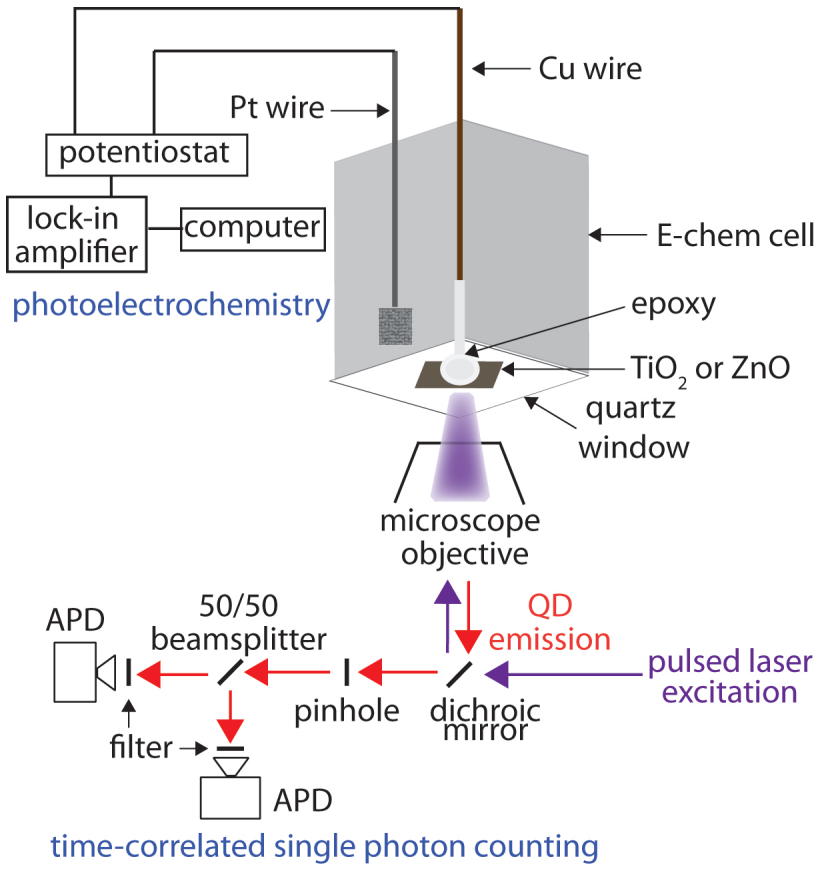

Figure 35: Experimental Setup for Photoluminescence Decay Measurements Experimental setup for photoluminescence decay measurements of QDSSCs at short-circuit.

5.3 Results and Discussion

In order to directly compare the sensitized photocurrent yields it is important to determine the QD surface coverage. Figure 36 shows AFM images of TiO_2 and ZnO before and after adsorption of MPA-, MUA-, OA- or TOPO-capped CdSe QDs. Bare rutile (110) TiO_2 (figure 36a) exhibited flat terraces with an average width of 70 nm (residual silica particles seen in this image from polishing can be removed with HF immersion) whereas the clean ZnO (0001) surface (figure 36e) exhibited a root mean square roughness of 0.1 nm without well-defined terraces. Due to the bifunctional chemical moieties used to chemically bind MPA (figure 36b and 36f) and MUA-capped (figure 36c and 36g) QDs to the oxide surface, these QDs predominantly adsorb in a single layer on TiO2 and ZnO. However some regions of the TiO_2 crystal exhibited MPA-QD clusters consisting of 3 or more nanocrystals (figure 37). In contrast, QDs capped with bulky OA or TOPO ligands (figure 36d and 36h) form large clusters with varying surface coverage at least partly because surface chemical bonds are not formed between OA or TOPO-capped QDs and the metal oxide surfaces. The surface morphology of the QDs studied herein agree well with previous studies using thoroughly washed aqueous MPA-QD samples[56, 100].

Figures 38a and 38b show the incident photon-to-current efficiency (IPCE) spectra of single crystal TiO_2 or ZnO electrodes sensitized with the same QD samples used for AFM measurements. The IPCE value at the first excitonic peak for MPA-capped QDs is 12.5 and 5.7 times larger than MUA-capped QDs on TiO_2 and ZnO, respectively. OA and TOPO-capped QDs showed negligible photocurrent generation on both substrates. It is evident that short alkyl chain bifunctional linker molecules (MPA) increase the electronic coupling between QD and substrate compared to long chain ligands. PL measurements previously demonstrated faster electron transfer rate constants for QDs capped with short chain ligands to TiO_2[105, 106, 113].

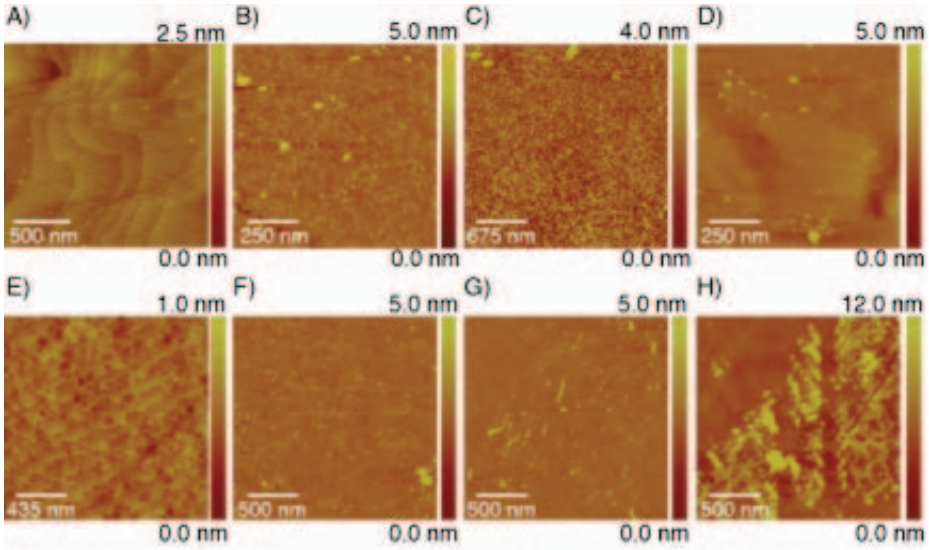

Figure 36: AFM Images of TiO_2 and ZnO
AFM images of A) bare rutile TiO_2 (110) and after 1 hr immersion in B) ON-MPA QDs, C), synthesized MUA-QDs and D) ON-TOPO-QDs. E) bare ZnO (0001) and after 1 hr immersion in F) synthesized MPA-capped, G) synthesized MUA-capped and H) synthesized OA-capped QDs.

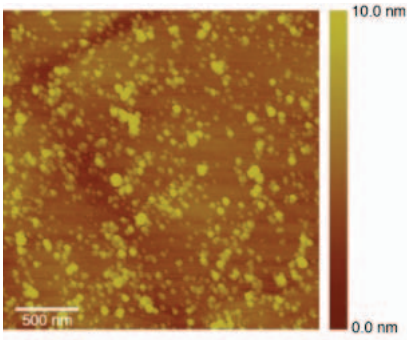

Figure 37: AFM Images of MPA-capped NC Clusters
AFM images of clusters of MPA-QDs on TiO_2. The average cluster has a radius of 75 nm.

A

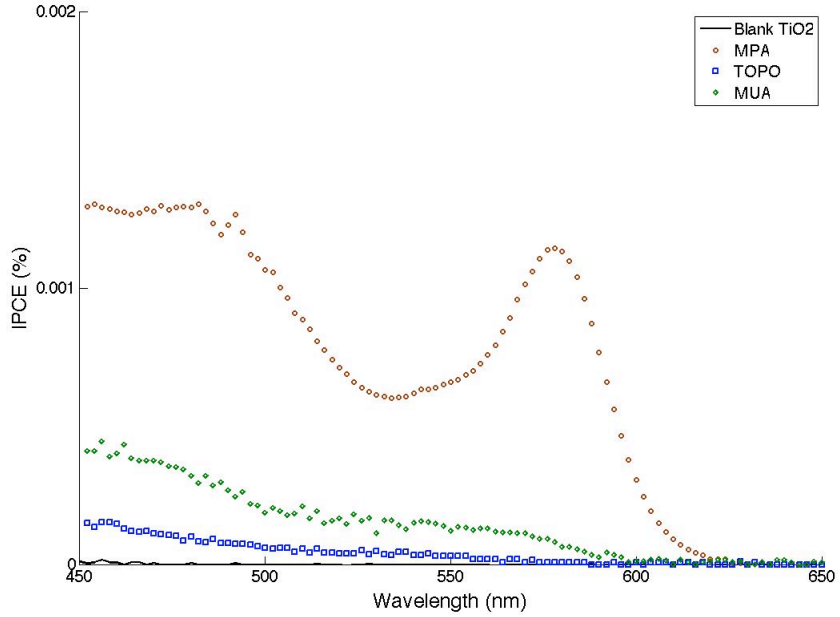

B

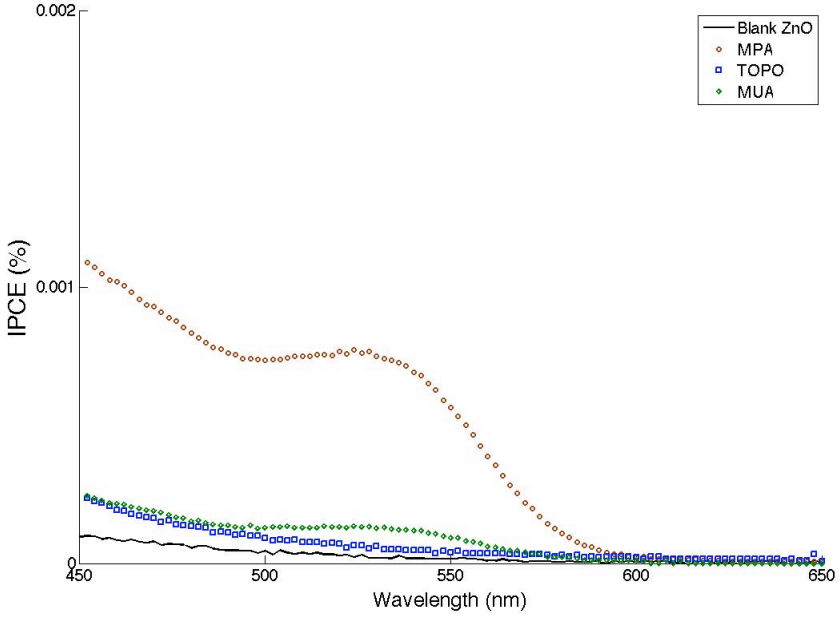

Figure 38: IPCE of Sensitized TiO_2 and ZnO

IPCE spectra of a) a rutile (110) TiO_2 single crystal electrode sensitized with MPA ON-QDs, TOPO ON-QDs and synthesized MUA-QDs (acquired in 0.5 M Na_2S in 0.1 M NaOH) at short circuit in a two-electrode configuration versus a platinum wire) and b) a ZnO (0001) single crystal electrode sensitized with synthesized MPA, MUA and TOPO QDs.

Time-correlated single photon counting (TCSPC) was used to measure the photoluminescence (PL) decay of QDs in solution, adsorbed on glass or adsorbed on single crystal oxides. Figure 39a shows that the PL decay of solubilized MPA- and MUA-capped CdSe QDs are quenched compared to the TOPO or OA-capped CdSe QDs, a well-known effect of capping CdSe QD with thiols[160]. An aliquot of each solution was then dried on a glass cover slip and the PL decay traces were measured (figure 39b). All of the PL decays are fit to

$$I(t) = Ae^{-t/\tau_1} + Be^{-t/\tau_2} \tag{24}$$

after deconvulation with the instrument response function (figure 41) and summarized for each type of ligand in table 6. The PL lifetimes are quenched on the glass substrate compared to solution, particularly for the OA and TOPO-capped QDs. The multi-exponential photoluminescence decay is due to the lack of a shell and chemical modifications to the CdSe QDs. For comparison, the photoluminescence decay from high quantum yield TOPO-capped CdSe/ZnS is shown in Section 4.3. Figure 40a and 40b show the PL decay of the MPA-, MUA-, OA- and TOPO-capped QDs on TiO_2 and ZnO, respectively. All of the PL decays in figures 40a and 40b were obtained in the same electrolyte and short-ciruit configuration as the IPCE measurements, so that we are measuring the photoresponse of the QDs in the same surrounding environment as the IPCE measurements. Notably, all samples show quenched PL decays relative to those in figure 39a, which is quantified by fitting the PL decays to eq 24, summarized in table 7. Of particular note is that for the TiO_2 sensitized with TOPO-capped QDs, the PL decay rate is quenched to a higher degree than any other sample.

A

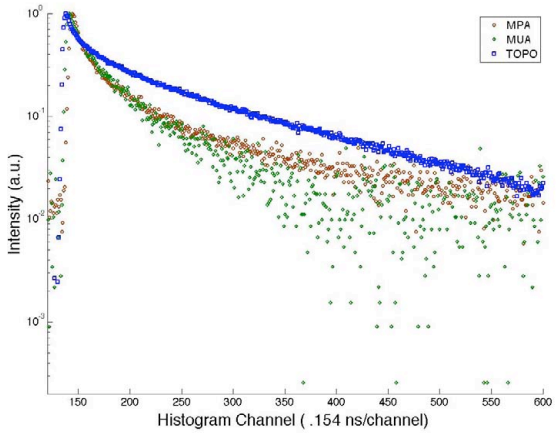

B

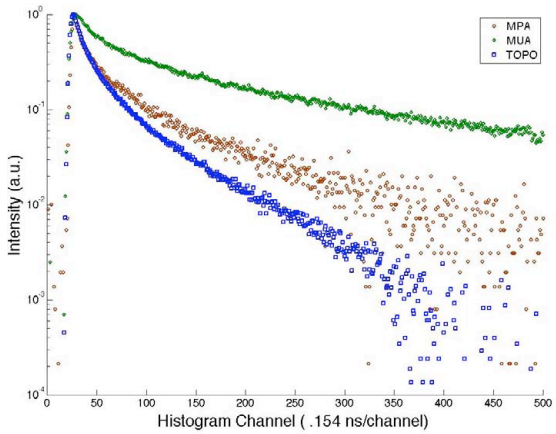

Figure 39: PL Decay of QDs in Solution and Deposited on Glass
PL Decay for MPA,- MUA-, and TOPO-capped CdSe QDs in (A) solution and (B) on glass (deposited with the same procedure as the TiO_2 and ZnO substrates), taking into account the instrument response function (figure 41).

Ligand		**Solution**	**Glass**
MPA	τ_1	4.7 ns	0.9 ns
	τ_2	17.2 ns	6.9 ns
MUA	τ_1	3.5 ns	2.8 ns
	τ_2	16.7 ns	11.6 ns
TOPO/OA	τ_1	4.0 ns	0.7 ns
	τ_2	16.4 ns	5.5 ns

Table 6: Results of Fitting PL Decays in Figure 39
Photoluminescence decay rates obtained by fitting the photoluminescence decays in figure 39a and 39b to eq 24.

A

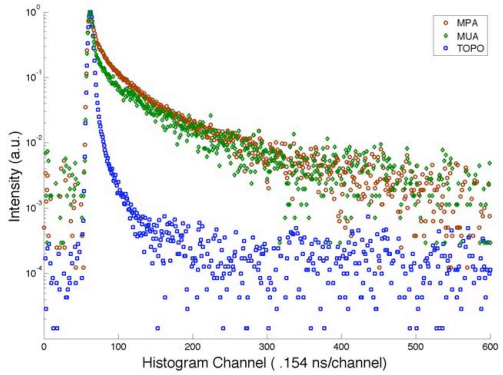

B

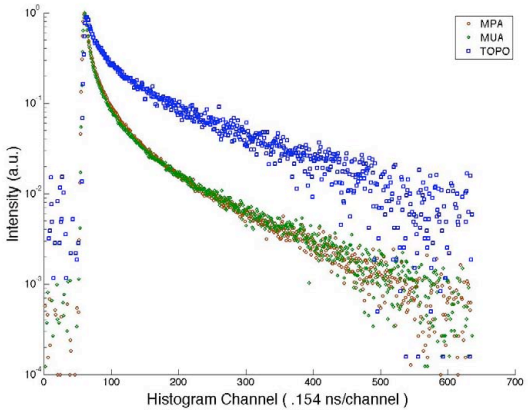

Figure 40: PL Decay of QD sensitized TiO_2 and ZnO
PL Decay for MPA, MUA, and TOPO-capped CdSe QDs on (A) TiO_2, and (B) ZnO. All decays are fit to eq 24, taking into account the instrument response function (figure 41).

Ligand		**TiO_2**	**ZnO**
MPA	τ_1	0.4 ns	0.7 ns
	τ_2	1.7 ns	5.2 ns
MUA	τ_1	0.3 ns	0.6 ns
	τ_2	16.7 ns	5.0 ns
TOPO/OA	τ_1	0.3 ns	0.8 ns
	τ_2	2.0 ns	7.5 ns

Table 7: Results of Fitting PL Decays in Figure 40
Photoluminescence decay rates obtained by fitting the photoluminescence decays in figure 40a and 40b to eq 24.

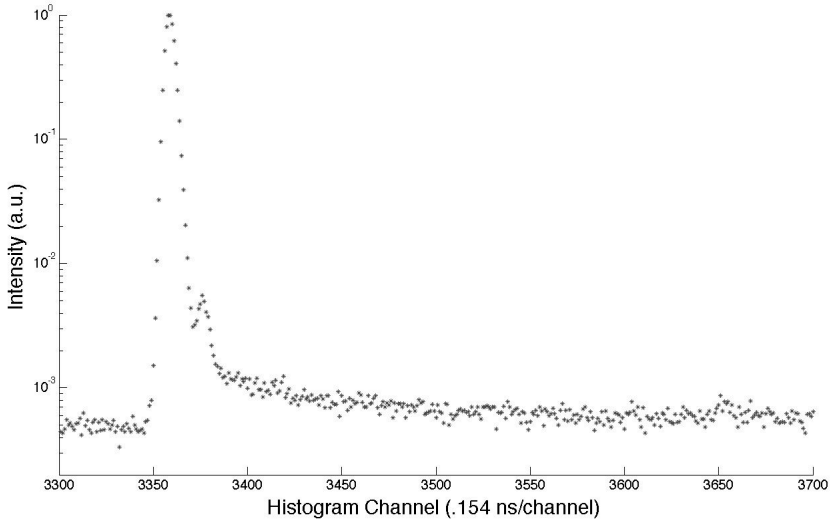

Figure 41: Instrument Response Function
The measured instrument response function for all photoluminescence decay histograms presented in this chapter. The secondary peak is an inherent feature of our system, due to timing electronics.

Quenching of the QD PL lifetime is generally interpreted as electron injection from the QD excited state to the oxide conduction band[91, 98, 105, 106]. Comparison of the photocurrent spectra and PL decay data indicates that this interpretation can be misleading. Although the PL lifetime is quenched for all samples, the photocurrent spectra are highly ligand-dependent. Most notably, the TOPO-capped sample shows the highest percentage of quenching in the lifetime(s) despite essentially no sensitized photocurrent.

What factors account for the disparity between photoelectrochemical and time-resolved PL measurements in QD-sensitized metal oxide systems? Photocurrent measurements accurately quantify injected electrons by measuring current flow in an external circuit. Time-resolved PL measurements rely on radiative recombination events to indicate the rate of electron transfer and thus are an indirect measurement. Several possible explanations to account for the quenched PL data are discussed below. Given the similar initial lifetimes in solution, with small differences due to quench-

ing from the thiol ligands[45], we must assume that QD-substrate coupling is not the only process that can quench the fluorescence lifetime. Possible sources of this quenching are QD-QD interactions[82, 110], QD charging[70], and QD-electrolyte interactions[20, 45, 172, 173]. While QD-electrolyte interactions are mediated by different surface ligands[20, 45, 172, 173], we see no difference between fluorescence decays of all three types of QDs in dilute solution of electrolyte (figure 42).

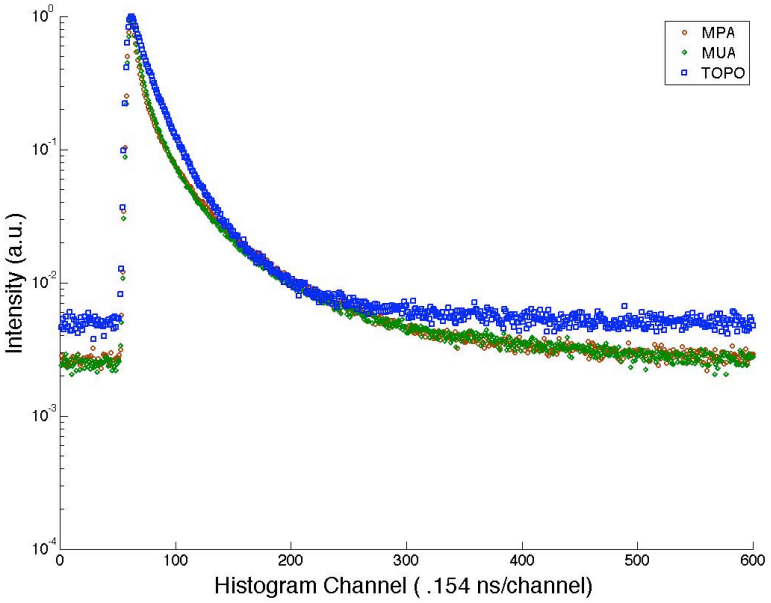

Figure 42: PL Decay of CdSe QDs in Dilute Electrolyte
PL Decay for MPA, MUA, and TOPO-capped CdSe QDs in dilute sulphide electrolyte. All decays are fit to eq 24, taking into account the instrument response function (figure 41).

However, QD-QD interactions have been shown to greatly influence the flow of energy in coupled systems. On insulating substrates, we have shown that small clusters of core-shell QDs interact, causing a reduction in lifetime and variations in the blinking pattern[31, 82]. The Bonn group proposed that similar clusters of PbSe QDs found in PbSe QD – TiO_2 nanoparticle slurries may be detrimental to the overall performance of the device, postulating a similar mechanism to our results[110]. As shown in figure 36g, the TOPO-capped QDs tend to form clusters on the surface

of both substrates, which suggests that QD-QD interactions are responsible for the lifetime quenching rather than charge transfer to the semiconducting substrate. Additionally, it is likely that charge transfer can also occur from the QD or QD trap states to a surface trap state on the semiconducting substrate[46, 70]. It is easy to extend both of these interactions to see how one QD in a cluster may become charged, and therefore become a non-radiative recombination center[70], and then other QDs in close proximity are quenched by energy transfer to this non-radiative recombination center. This process is also possible with the mercaptoalkyl acid(MAA)-capped QDs, but the rate of charge transfer to the semiconducting substrates is much faster than for the TOPO-capped QDs and the MAA-capped QDs tend to form well-dispersed monolayers, limiting the amount of QD-QD interactions.

5.4 Conclusion

We have observed changes in the photoluminescence decay of TOPO-capped CdSe QDs deposited on single crystal ZnO and TiO_2 that match the signatures of efficient charge transfer, yet these samples show no sensitization in IPCE measurements. MPA- and MUA-capped CdSe QDs show similar changes in photoluminescence decay once deposited onto ZnO or TiO_2, but contrary to the TOPO-capped QDs the IPCE measurements confirm charge transfer from the QDs producing a sensitized current in the semiconductor. The exact mechanism responsible for quenching of the photoluminescence in the TOPO-capped QDs remains unknown. However, electronic coupling between adjacent and similar-sized QDs (with bulky organic ligands) has been reported in the literature and it also is possible that interaction with static traps in the semiconductor may alter the radiative rate[31, 82, 110]. Going forward, we suggest that future experiments investigating the time dynamics of charge separation in QDSSCs independently confirm charge transfer through IPCE and J-V measurements.

6 Perspective

Our work here began with an effort to clarify the mechanism of the enhanced blinking of clusters of semiconductor core-shell spherical NCs originally reported by Dr. Ming Chen in 2006[31]. By utilizing the extended capabilities of time-correlated single photon, we measured the photoluminescence decay rate of small NC clusters and correlated it to changes in photoluminescence intensity. After analyzing fluorescence-intensity lifetime distributions and creating a simple kinetic rate model, we posited that energy transfer between these close packed NCs is responsible for the characteristic PL properties of enhanced blinking[82]. Because this energy transfer only effects the excited state of the NCs, there remains an open question if the fundamental processes that govern blinking are altered. Recent work in our group by Kevin Whitcomb indicate that a statistical analysis of long time (≈20 minutes) fluorescence trajectories shows no difference in *on*/*off* probability distributions and multi-generation *on*/*off* correlations. These early results imply that the individual NCs in the cluster continue independently blink even when close enough for efficient energy transfer to significantly alter the fluorescence trajectory. Based on these results, the term "enhanced blinking" may be a misnomer and a better term may be "FRET-mediated blinking".

We propose that these interactions may lead to "energy sinks", where energy transfer occurs between a donor NC and a acceptor NC in the *off* state. This raises the point that NC based devices relying coupling between NCs may be effected by these inter-NC interactions. Because it is impossible to measure thin films of NCs without averaging over many NCs, we were unable to verify this until we began to investi-

gate CdSe quantum dot single crystal sensitized solar cells in collaboration with the Parkinson group at the University of Wyoming. Our initial hope was to correlate photoluminescence intensity and decay rates with varying surface morphology on the substrate and the effect of varying the capping ligands. The Parkinson group has shown through photocurrent measurements and atomic force microscopy that the substrate preparation and ligand chemistry govern the quality of NC dispersion and photovoltaic performance[135]. A side product of these AFM images was the observation that there existed both isolated individual NCs, small NC clusters, and large NC clusters on the substrate surface. Because of the low quantum yield of NCs coupled to semiconducting substrates, we were forced to average our PL measurements over larger areas on the sample surface. To offset this, we compared the photocurrent response of NCs with capping ligands that simultaneously promote charge transfer and limit clustering versus ligands that limit charge transfer and promote clustering. We found in both cases that the lifetime of the NCs is significantly altered compared to native NCs in solution, despite essentially no photocurrent from NCs capping by ligands that promote clustering. Given our results that inter-NC interactions in small clusters shortens the average lifetime and recent results from the Bonn group that clustering of NCs may mimic charge injection in a similar system[110], we propose that a reduction in the photoluminescence decay rate long associated with charge injection in NC sensitized solar cells[104] may not solely be due to charge injection and is a poor predictor of device performance.

In the near future, we have two seemingly two divergent experimental needs. The first focuses on understanding the basic interactions of closely packed NCs in isolated clusters. As previously mentioned, Kevin Whitcomb has started on this already by collecting long time fluorescence trajectories for statistical analysis. The most important goal here is to measure the number of NCs in a cluster. The Drndic group has accomplished this for semiconducting nanorods, by correlating TEM and

photoluminescence measurements[141] and we have an active collaboration with their group to understand if our experiments are possible with their TEM grids. Another possible method is to synthetically control the number of NCs in cluster a through ligand chemistry. With the help of Shannon Riha in the Prieto Group, we attempted to synthesize QD dimers following a procedure developed by the Shumaker-Parry group[174]. While we were succesful at creating dimers of different sized CdSe/ZnS quantum dots, the dimers were only photostable for minutes in solution. Despite our attempts to solve this issue, we remain unsuccesful to this point.

The second focuses on studying the effects of inter-NC coupling in single crystal QDSSCs further. We have already shown that NC clusters may be responsible for a quenching of photoluminescence decay rates in the abscence of charge transfer. The next step is to interrogate both isolated individual NCs and small NC clusters separately on various semiconducting surfaces. Only by understanding how the individual components act in these systems will we be able to understand why the only reported success at harvesting multiple charge carriers per photon has been reported in QD coupled to single crystal semiconducting substrates[101].

Continued development of our "bottom-up" or "non-ensemble" approach to these open scientific problems will provide this information at the single particle level, complimenting ultra-fast optical techniques to guide the development of NC based devices.

References

[1] Ekimov, A.; Efros, A.; Onushchenko, A. *Solid State Commun.* **1993**, *88*, 947–950.

[2] Alivisatos, A. P. *Science* **1996**, *271*, 933 –937.

[3] Alivisatos, A. P.; Gu, W.; Larabell, C. *Annu. Rev. Biomed. Eng.* **2005**, *7*, 55–76.

[4] Gerding, J. D.; Willard, D. M.; Orden, A. V. *J. Am. Chem. Soc.* **2005**, *127*, 1106–1107.

[5] Gerion, D.; Pinaud, F.; Williams, S. C.; Parak, W. J.; Zanchet, D.; Weiss, S.; Alivisatos, A. P. *J. Phys. Chem. B* **2001**, *105*, 8861–8871.

[6] Medintz, I. L.; Uyeda, H. T.; Goldman, E. R.; Mattoussi, H. *Nat. Mater.* **2005**, *4*, 435–446.

[7] Caruge, J. M.; Halpert, J. E.; Wood, V.; Bulovic, V.; Bawendi, M. G. *Nat. Photon.* **2008**, *2*, 247–250.

[8] Eisler, H.; Sundar, V. C.; Bawendi, M. G.; Walsh, M.; Smith, H. I.; Klimov, V. *Appl. Phys. Lett.* **2002**, *80*, 4614.

[9] Ivanov, S. A.; Nanda, J.; Piryatinski, A.; Achermann, M.; Balet, L. P.; Bezel, I. V.; Anikeeva, P. O.; Tretiak, S.; Klimov, V. I. *J. Phys. Chem. B* **2004**, *108*, 10625–10630.

[10] Klimov, V. I.; Mikhailovsky, A. A.; Xu, S.; Malko, A.; Hollingsworth, J. A.; Leatherdale, C. A.; Eisler, H.; Bawendi, M. G. *Science* **2000**, *290*, 314 –317.

[11] Klimov, V. I.; Ivanov, S. A.; Nanda, J.; Achermann, M.; Bezel, I.; McGuire, J. A.; Piryatinski, A. *Nature* **2007**, *447*, 441–446.

[12] Clifford, J. P.; Konstantatos, G.; Johnston, K. W.; Hoogland, S.; Levina, L.; Sargent, E. H. *Nat. Nano.* **2009**, *4*, 40–44.

[13] Sukhovatkin, V.; Hinds, S.; Brzozowski, L.; Sargent, E. H. *Science* **2009**, *324*, 1542–1544.

[14] Kamat, P. V. *J. Phys. Chem. C* **2008**, *112*, 18737–18753.

[15] Pattantyus-Abraham, A. G.; Kramer, I. J.; Barkhouse, A. R.; Wang, X.; Konstantatos, G.; Debnath, R.; Levina, L.; Raabe, I.; Nazeeruddin, M. K.; Grätzel, M.; Sargent, E. H. *ACS Nano* **2010**, *4*, 3374–3380.

[16] Burda, C.; Chen, X.; Narayanan, R.; El-Sayed, M. A. *Chem. Rev.* **2005**, *105*, 1025–1102.

[17] He, H.; Qian, H.; Dong, C.; Wang, K.; Ren, J. *Angew. Chem. Int. Edit.* **2006**, *118*, 7750–7753.

[18] Murray, C. B.; Sun, S.; Gaschler, W.; Doyle, H.; Betley, T. A.; Kagan, C. R. *IBM J. Res. Dev.* **2001**, *45*, 47–56.

[19] Yin, Y.; Alivisatos, A. P. *Nature* **2005**, *437*, 664–670.

[20] Algar, W. R.; Krull, U. J. *ChemPhysChem* **2007**, *8*, 561–568.

[21] Moerner, W. E.; Fromm, D. P. *Rev. Sci. Instrum.* **2003**, *74*, 3597.

[22] Ambrose, W. P.; Goodwin, P. M.; Jett, J. H.; Orden, A. V.; Werner, J. H.; Keller, R. A. *Chem. Rev.* **1999**, *99*, 2929–2956.

[23] Ha, T.; Enderle, T.; Ogletree, D. F.; Chemla, D. S.; Selvin, P. R.; Weiss, S. *P. Natl. Acad. Sci.* **1996**, *93*, 6264–6268.

[24] Becker, W.; Bergmann, A.; Hink, M. A.; König, K.; Benndorf, K.; Biskup, C. *Microsc. Res. Techniq.* **2004**, *63*, 58–66.

[25] Enderlein, J.; Sauer, M. *J. Phys. Chem. A* **2001**, *105*, 48–53.

[26] Huang, B.; Jones, S. A.; Brandenburg, B.; Zhuang, X. *Nat. Methods* **2008**, *5*, 1047–1052.

[27] Zhuang, X. *Nat. Photonics* **2009**, *3*, 365–367.

[28] Klimov, V. I. *J. Phys. Chem. B* **2000**, *104*, 6112–6123.

[29] Cho, B.; Peters, W. K.; Hill, R. J.; Courtney, T. L.; Jonas, D. M. *Nano Lett.* **2010**, *10*, 2498–2505.

[30] Nair, G. P.; Ph.D. thesis; Massachusetts Institute of Technology; 2009.

[31] Yu, M.; Orden, A. V. *Phys. Rev. Lett.* **2006**, *97*, 237402.

[32] Pong, B.; Trout, B. L.; Lee, J. *Langmuir* **2008**, *24*, 5270–5276.

[33] Hines, M. A.; Guyot-Sionnest, P. *J. Phys. Chem.* **1996**, *100*, 468–471.

[34] Reiss, P.; Protière, M.; Li, L. *Small* **2009**, *5*, 154–168.

[35] Tang, Z.; Ozturk, B.; Wang, Y.; Kotov, N. A. *J. Phys. Chem. B* **2004**, *108*, 6927–6931.

[36] Franzl, T.; Shavel, A.; Rogach, A. L.; Gaponik, N.; Klar, T. A.; Eychmüller, A.; Feldmann, J. *Small* **2005**, *1*, 392–395.

[37] Higgins, C.; Lunz, M.; Bradley, A. L.; Gerard, V. A.; Byrne, S.; Gunko, Y. K.; Lesnyak, V.; Gaponik, N. *Opt. Express* **2010**, *18*, 24486–24494.

[38] Nirmal, M.; Dabbousi, B. O.; Bawendi, M. G.; Macklin, J. J.; Trautman, J. K.; Harris, T. D.; Brus, L. E. *Nature* **1996**, *383*, 802–804.

[39] Empedocles, S. A.; Norris, D. J.; Bawendi, M. G. *Phys. Rev. Lett.* **1996**, *77*, 3873.

[40] Empedocles, S. A.; Bawendi, M. G. *Science* **1997**, *278*, 2114–2117.

[41] Kuno, M.; Fromm, D. P.; Hamann, H. F.; Gallagher, A.; Nesbitt, D. J. *J. Chem. Phys.* **2001**, *115*, 1028.

[42] Fisher, B. R.; Eisler, H.; Stott, N. E.; Bawendi, M. G. *J. Phys. Chem. B* **2004**, *108*, 143–148.

[43] Chan, W. C. W.; Nie, S. *Science* **1998**, *281*, 2016 –2018.

[44] Peng, Z. A.; Peng, X. *J. Am. Chem. Soc.* **2000**, *123*, 183–184.

[45] Aldana, J.; Wang, Y. A.; Peng, X. G. *J. Am. Chem. Soc.* **2001**, *123*, 8844–8850.

[46] Smith, A. M.; Duan, H.; Rhyner, M. N.; Ruan, G.; Nie, S. *Phys. Chem. Chem. Phys.* **2006**, *8*, 3895.

[47] Klimov, V. I.; McBranch, D. W.; Leatherdale, C. A.; Bawendi, M. G. *Phys. Rev. B* **1999**, *60*, 13740.

[48] Klimov, V. I.; Mikhailovsky, A. A.; McBranch, D. W.; Leatherdale, C. A.; Bawendi, M. G. *Science* **2000**, *287*, 1011 –1013.

[49] Wang, L. *Phys. Rev. B* **1996**, *53*, 9579–9582.

[50] Margolin, G.; Protasenko, V.; Kuno, M.; Barkai, E. *Adv, Chem. Phys. A* **2006**, 327–356.

[51] Empedocles, S.; Bawendi, M. *Accounts Chem. Res.* **1999**, *32*, 389–396.

[52] Norris, D. J.; Bawendi, M. G. *Phys. Rev. B* **1996**, *53*, 16338.

[53] Wagner, P. J. *Accounts Chem. Res.* **1983**, *16*, 461–467.

[54] Guillemoles, J.; Barone, V.; Joubert, L.; Adamo, C. *J. Phys. Chem. A* **2002**, *106*, 11354–11360.

[55] Leatherdale, C. A.; Woo, W.; Mikulec, F. V.; Bawendi, M. G. *J. Phys. Chem. B* **2002**, *106*, 7619–7622.

[56] Yu, W. W.; Qu, L. H.; Guo, W. Z.; Peng, X. G. *Chem. Mater.* **2003**, *15*, 2854–2860.

[57] Nozik, A. J. *Chem. Phys. Lett.* **2008**, *457*, 3–11.

[58] Efros, A. L.; Rosen, M.; Kuno, M.; Nirmal, M.; Norris, D. J.; Bawendi, M. *Phys. Rev. B* **1996**, *54*, 4843.

[59] Kuno, M.; Lee, J. K.; Dabbousi, B. O.; Mikulec, F. V.; Bawendi, M. G. *J. Chem. Phys.* **1997**, *106*, 9869.

[60] Nirmal, M.; Norris, D. J.; Kuno, M.; Bawendi, M. G.; Efros, A. L.; Rosen, M. *Phys. Rev. Lett.* **1995**, *75*, 3728.

[61] Norris, D. J.; Efros, A. L.; Rosen, M.; Bawendi, M. G. *Phys. Rev. B* **1996**, *53*, 16347.

[62] Kuno, M.; Fromm, D. P.; Johnson, S. T.; Gallagher, A.; Nesbitt, D. J. *Phys. Rev. B* **2003**, *67*, 125304.

[63] Jha, P. P.; Guyot-Sionnest, P. *ACS Nano* **2009**, *3*, 1011–1015.

[64] Frantsuzov, P.; Kuno, M.; Janko, B.; Marcus, R. A. *Nat. Phys.* **2008**, *4*, 519–522.

[65] Efros, A. L. *Nat. Mater.* **2008**, *7*, 612–613.

[66] Kuno, M.; Fromm, D. P.; Hamann, H. F.; Gallagher, A.; Nesbitt, D. J. *J. Chem. Phys.* **2000**, *112*, 3117.

[67] Volkan-Kacso, S.; Frantsuzov, P. A.; Janko, B. *Nano Lett.* **2010**, *10*, 2761–2765.

[68] Margolin, G.; Protasenko, V.; Kuno, M.; Barkai, E. *J. Phys. Chem. B* **2006**, *110*, 19053–19060.

[69] Krauss, T. D.; Peterson, J. J. *J. Phys. Chem. Lett.* **2010**, *1*, 1377–1382.

[70] Li, S.; Steigerwald, M. L.; Brus, L. E. *ACS Nano* **2009**, *3*, 1267–1273.

[71] Mahler, B.; Spinicelli, P.; Buil, S.; Quelin, X.; Hermier, J.; Dubertret, B. *Nat. Mater.* **2008**, *7*, 659–664.

[72] Zhao, J.; Nair, G.; Fisher, B. R.; Bawendi, M. G. *Phys. Rev. Lett.* **2010**, *104*, 157403.

[73] Beard, M. C.; Turner, G. M.; Murphy, J. E.; Micic, O. I.; Hanna, M. C.; Nozik, A. J.; Schmuttenmaer, C. A. *Nano Lett.* **2003**, *3*, 1695–1699.

[74] Talapin, D. V.; Murray, C. B. *Science* **2005**, *310*, 86–89.

[75] Luther, J.; Law, M.; Beard, M.; Song, Q.; Reese, M.; Ellingson, R.; Nozik, A. *Nano Lett.* **2008**, *8*, 3488–3492.

[76] Beard, M. C.; Midgett, A. G.; Law, M.; Semonin, O. E.; Ellingson, R. J.; Nozik, A. J. *Nano Lett.* **2009**, *9*, 836–845.

[77] Nozik, A. J.; Beard, M. C.; Luther, J. M.; Law, M.; Ellingson, R. J.; Johnson, J. C. *Chem. Rev.* **2010**, *110*, 6873–6890.

[78] Kagan, C. R.; Murray, C. B.; Bawendi, M. G. *Phys. Rev. B* **1996**, *54*, 8633.

[79] Franzl, T.; Koktysh, D. S.; Klar, T. A.; Rogach, A. L.; Feldmann, J.; Gaponik, N. *Appl. Phys. Lett.* **2004**, *84*, 2904.

[80] Lee, J.; Govorov, A. O.; Kotov, N. A. *Nano Lett.* **2005**, *5*, 2063–2069.

[81] Koole, R.; Liljeroth, P.; de Mello Donegá, C.; Vanmaekelbergh, D.; Meijerink, A. *J. Am. Chem. Soc.* **2006**, *128*, 10436–10441.

[82] Shepherd, D. P.; Whitcomb, K. J.; Milligan, K. K.; Goodwin, P. M.; Gelfand, M. P.; Orden, A. V. *J. Phys. Chem. C* **2010**, *114*, 14831–14837.

[83] Förster, T. *Radiat. Res.* **1960**, *2*, 326–339.

[84] Ha, T. *Methods* **2001**, *25*, 78–86.

[85] Pons, T.; Medintz, I. L.; Wang, X.; English, D. S.; Mattoussi, H. *J. Am. Chem. Soc.* **2006**, *128*, 15324–15331.

[86] Pons, T.; Medintz, I. L.; Sykora, M.; Mattoussi, H. *Phys. Rev. B* **2006**, *73*, 245302.

[87] Kubin, R. F.; Fletcher, A. N. *J. Lumin.* **1982**, *27*, 455–462.

[88] Willard, D. M.; Carillo, L. L.; Jung, J.; Orden, A. V. *Nano Lett.* **2001**, *1*, 469–474.

[89] Zaban, A.; Micic, O. I.; Gregg, B. A.; Nozik, A. J. *Langmuir* **1998**, *14*, 3153–3156.

[90] Plass, R.; Pelet, S.; Krueger, J.; Grätzel, M.; Bach, U. *J. Phys. Chem. B* **2002**, *106*, 7578–7580.

[91] Robel, I.; Subramanian, V.; Kuno, M.; Kamat, P. V. *J. Am. Chem. Soc.* **2006**, *128*, 2385–2393.

[92] Gur, I.; Fromer, N. A.; Chen, C.; Kanaras, A. G.; Alivisatos, A. P. *Nano Lett.* **2006**, *7*, 409–414.

[93] Johnston, K. W.; Pattantyus-Abraham, A. G.; Clifford, J. P.; Myrskog, S. H.; Hoogland, S.; Shukla, H.; Klem, E. J. D.; Levina, L.; Sargent, E. H. *Appl. Phys. Lett.* **2008**, *92*, 122111.

[94] Sun, W.; Yu, Y.; Pan, H.; Gao, X.; Chen, Q.; Peng, L. *J. Am. Chem. Soc.* **2008**, *130*, 1124–1125.

[95] Lee, H.; Leventis, H. C.; Moon, S.; Chen, P.; Ito, S.; Haque, S. A.; Torres, T.; Nüesch, F.; Geiger, T.; Zakeeruddin, S. M.; Grätzel, M.; Nazeeruddin, M. K. *Adv. Func. Mater.* **2009**, *19*, 2735–2742.

[96] Lee, H.; Chen, P.; Moon, S.; Sauvage, F.; Sivula, K.; Bessho, T.; Gamelin, D.; Comte, P.; Zakeeruddin, S.; Seok, S.; Grätzel, M.; Nazeeruddin, M. *Langmuir* **2009**, *25*, 7602–7608.

[97] Leschkies, K. S.; Beatty, T. J.; Kang, M. S.; Norris, D. J.; Aydil, E. S. *ACS Nano* **2009**, *3*, 3638–3648.

[98] Acharya, K. P.; Hewa-Kasakarage, N. N.; Alabi, T. R.; Nemitz, I.; Khon, E.; Ullrich, B.; Anzenbacher, P.; Zamkov, M. *J. Phys. Chem. C* **2010**, *114*, 12496–12504.

[99] Kamat, P. V.; Tvrdy, K.; Baker, D. R.; Radich, J. G. *Chem. Rev.* **2010**, *110*, 6664–6688.

[100] Sambur, J. B.; Parkinson, B. A. *J. Am. Chem. Soc.* **2010**, *132*, 2130–2131.

[101] Sambur, J. B.; Novet, T.; Parkinson, B. A. *Science* **2010**, *330*, 63–66.

[102] Tachibana, Y.; Moser, J. E.; Gratzel, M.; Klug, D. R.; Durrant, J. R. *J. Phys. Chem.* **1996**, *100*, 20056–20062.

[103] Boulesbaa, A.; Issac, A.; Stockwell, D.; Huang, Z.; Huang, J.; Guo, J.; Lian, T. *J. Am. Chem. Soc.* **2007**, *129*, 15132–15133.

[104] Hyun, B.; Zhong, Y.; Bartnik, A. C.; Sun, L.; Abruna, H. D.; Wise, F. W.; Goodreau, J. D.; Matthews, J. R.; Leslie, T. M.; Borrelli, N. F. *ACS Nano* **2008**, *2*, 2206–2212.

[105] Dibbell, R. S.; Watson, D. F. *J. Phys. Chem. C* **2009**, *113*, 3139–3149.

[106] Jin, S.; Lian, T. *Nano Lett.* **2009**, *9*, 2448–2454.

[107] Boulesbaa, A.; Huang, Z.; Wu, D.; Lian, T. *J. Phys. Chem. C* **2010**, *114*, 962–969.

[108] Guijarro, N.; Shen, Q.; Gimenez, S.; Mora-Sero, I.; Bisquert, J.; Lana-Villarreal, T.; Toyoda, T.; Gomez, R. *J. Phys. Chem. C* **2010**, *114*, 22352–22360.

[109] Leventis, H. C.; O'Mahony, F.; Akhtar, J.; Afzaal, M.; O'Brien, P.; Haque, S. A. *J. Am. Chem. Soc.* **2010**, *132*, 2743–2750.

[110] Pijpers, J. J. H.; Koole, R.; Evers, W. H.; Houtepen, A. J.; Boehme, S.; de Mello Donegar, C.; Vanmaekelbergh, D.; Bonn, M. *J. Phys. Chem. C* **2010**, *114*, 18866–18873.

[111] Rawalekar, S.; Kaniyankandy, S.; Verma, S.; Ghosh, H. N. *J. Phys. Chem. C* **2010**, *114*, 1460–1466.

[112] Stockwell, D.; Yang, Y.; Huang, J.; Anfuso, C.; Huang, Z.; Lian, T. *J. Phys. Chem. C* **2010**, *114*, 6560–6566.

[113] Kongkanand, A.; Tvrdy, K.; Takechi, K.; Kuno, M.; Kamat, P. V. *J. Am. Chem. Soc.* **2008**, *130*, 4007–4015.

[114] Tamarat, P.; Maali, A.; Lounis, B.; Orrit, M. *J. Phys. Chem. A* **2000**, *104*, 1–16.

[115] Webb, W. W. *Appl. Optics* **2001**, *40*, 3969–3983.

[116] Tinnefeld, P.; Sauer, M. *Angew. Chem. Int. Edit.* **2005**, *44*, 2642–2671.

[117] Jung, J.; Orden, A. V. *J. Am. Chem. Soc.* **2006**, *128*, 1240–1249.

[118] Bohmer, M.; Pampaloni, F.; Wahl, M.; Rahn, H.; Erdmann, R.; Enderlein, J. *Rev. Sci. Instrum.* **2001**, *72*, 4145.

[119] Benda, A.; Hof, M.; Wahl, M.; Patting, M.; Erdmann, R.; Kapusta, P. *Rev. Sci. Instrum.* **2005**, *76*, 033106.

[120] Kolodny, L. A.; Willard, D. M.; Carillo, L. L.; Nelson, M. W.; Orden, A. V. *Anal. Chem.* **2001**, *73*, 1959–1966.

[121] Schneckenburger, H. *Curr. Opin. Biotech.* **2005**, *16*, 13–18.

[122] Weiss, S. *Science* **1999**, *283*, 1676–1683.

[123] Paddock, S. W. *Mol. Biotech.* **2000**, *16*, 127–150.

[124] Pawley, J. B. *Handbook Of Biological Confocal Microscopy*; Springer US: Boston, MA, 2006.

[125] Wahl, M.; Rahn, H.; Gregor, I.; Erdmann, R.; Enderlein, J. *Rev. Sci. Instrum.* **2007**, *78*, 033106.

[126] Zhang, K.; Chang, H.; Fu, A.; Alivisatos, A. P.; Yang, H. *Nano Lett.* **2006**, *6*, 843–847.

[127] Hansma, P.; Elings, V.; Marti, O.; Bracker, C. *Science* **1988**, *242*, 209–216.

[128] García, R.; Pérez, R. *Surf. Sci. Rep.* **2002**, *47*, 197–301.

[129] Giessibl, F. J. *Rev. Mod. Phys.* **2003**, *75*, 949–983.

[130] Ebenstein, Y.; Nahum, E.; Banin, U. *Nano Lett.* **2002**, *2*, 945–950.

[131] Patolsky, F.; Gill, R.; Weizmann, Y.; Mokari, T.; Banin, U.; Willner, I. *J. Am. Chem. Soc.* **2003**, *125*, 13918–13919.

[132] Lu, H.; Schops, O.; Woggon, U.; Niemeyer, C. M. *J. Am. Chem. Soc.* **2008**, *130*, 4815–4827.

[133] Kan, H.; Tokumas, F.; Clark, M.; Zho, Z.; Tan, J.; Nguye, T.; Hwan, J. *Wiley Inter. Rev. Nanomed. Nanobio.* **2010**, *2*, 48–58.

[134] Medintz, I. L.; Mattoussi, H. *Phys. Chem. Chem. Phys.* **2009**, *11*, 17–45.

[135] Sambur, J. B.; Riha, S. C.; Choi, D.; Parkinson, B. A. *Langmuir* **2010**, *26*, 4839–4847.

[136] Kimura, J.; Maenosono, S.; Yamaguchi, Y. *Nanotechnology* **2003**, *14*, 69–72.

[137] Nozik, A. J. *Annu. Rev. Phys. Chem.* **2001**, *52*, 193–231.

[138] Pandey, A.; Guyot-Sionnest, P. *Science* **2008**, *322*, 929–932.

[139] Brokmann, X.; Marshall, L. F.; Bawendi, M. G. *Opt. Express* **2009**, *17*, 4509–4517.

[140] Kukura, P.; Celebrano, M.; Renn, A.; Sandoghdar, V. *Nano Lett.* **2008**, 926–929.

[141] Wang, S.; Querner, C.; Fischbein, M. D.; Willis, L.; Novikov, D. S.; Crouch, C. H.; Drndic, M. *Nano Lett.* **2008**, *8*, 4020–4026.

[142] Anni, M.; Manna, L.; Cingolani, R.; Valerini, D.; Creti, A.; Lomascolo, M. *Appl. Phys. Lett.* **2004**, *85*, 4169–4172.

[143] Funston, A. M.; Jasieniak, J. J.; Mulvaney, P. *Adv. Mater.* **2008**, *20*, 4274–4280.

[144] Dayal, S.; Lou, Y.; Samia, A. C. S.; Berlin, J. C.; Kenney, M. E.; Burda, C. *J. Am. Chem. Soc.* **2006**, *128*, 13974–13975.

[145] Robel, I.; Kuno, M.; Kamat, P. V. *J. Am. Chem. Soc.* **2007**, *129*, 4136–4137.

[146] Wargnier, R.; Baranov, A. V.; Maslov, V. G.; Stsiapura, V.; Artemyev, M.; Pluot, M.; Sukhanova, A.; Nabiev, I. *Nano Lett.* **2004**, *4*, 451–457.

[147] Guo, L.; Krauss, T. D.; Poitras, C. B.; Lipson, M.; Teng, X.; Yang, H. *Appl. Phys. Lett.* **2006**, *89*, 061104.

[148] Clark, S. W.; Harbold, J. M.; Wise, F. W. *J. Phys. Chem. C* **2007**, *111*, 7302–7305.

[149] Bose, R.; McMillan, J. F.; Gao, J.; Rickey, K. M.; Chen, C. J.; Talapin, D. V.; Murray, C. B.; Wong, C. W. *Nano Lett.* **2008**, *8*, 2006–2011.

[150] Curutchet, C.; Franceschetti, A.; Zunger, A.; Scholes, G. D. *J. Phys. Chem. C* **2008**, *112*, 13336–13341.

[151] Kagan, C. R.; Murray, C. B.; Nirmal, M.; Bawendi, M. G. *Phys. Rev. Lett.* **1996**, *76*, 1517.

[152] Tang, J.; Marcus, R. A. *J. Chem. Phys.* **2005**, *123*, 054704.

[153] Lee, Y.; Huang, B. M.; Chien, H. T. *Chem. Mater.* **2008**, *20*, 6903.

[154] Wang, X.; Ren, X.; Kahen, K.; Hahn, M. A.; Rajeswaran, M.; Maccagnano-Zacher, S.; Silcox, J.; Cragg, G. E.; Efros, A. L.; Krauss, T. D. *Nature* **2009**, *459*, 686–689.

[155] Lee, J. *Phys. Rev. B* **2009**, *80*, 205327–205332.

[156] Lee, H. J.; Yum, J.; Leventis, H. C.; Zakeeruddin, S. M.; Haque, S. A.; Chen, P.; Seok, S. I.; Gratzel, M.; Nazeeruddin, M. K. *J. Phys. Chem. C* **2008**, *112*, 11600–11608.

[157] Lounis, B.; Bechtel, H. A.; Gerion, D.; Alivisatos, P.; Moerner, W. E. *Chem. Phys. Lett.* **2000**, *329*, 399–404.

[158] Chan, W. C. W.; Maxwell, D. J.; Gao, X.; Bailey, R. E.; Han, M.; Nie, S. *Curr. Opin. Biotech.* **2002**, *13*, 40–46.

[159] Tang, J.; Marcus, R. A. *Phys. Rev. Lett.* **2005**, *95*, 107401.

[160] Aldana, J.; Lavelle, N.; Wang, Y. A.; Peng, X. G. *J. Am. Chem. Soc.* **2005**, *127*, 2496–2504.

[161] Luther, J. M.; Gao, J. B.; Lloyd, M. T.; Semonin, O. E.; Beard, M. C.; Nozik, A. J. *Adv. Mater.* **2010**, *22*, 3704–3710.

[162] Gao, J. B.; Luther, J. M.; Semonin, O. E.; Ellingson, R. J.; Nozik, A. J.; Beard, M. C. *Nano Lett.* **2011**, *11*, 1002–1008.

[163] Gur, I.; Fromer, N. A.; Geier, M. L.; Alivisatos, A. P. *Science* **2005**, *310*, 462–465.

[164] Zhou, Y.; Riehle, F. S.; Yuan, Y.; Schleiermacher, H.; Niggemann, M.; Urban, G. A.; Kruger, M. *Appl. Phys. Lett.* **2010**, *96*, 013304–3.

[165] Lokteva, I.; Radychev, N.; Witt, F.; Borchert, H.; Aàrgen Parisi, J.; Kolny-Olesiak, J. *J. Phys. Chem. C* **2010**, *114*, 12784–12791.

[166] Martinez-Ferrero, E.; Albero, J.; Palomares, E. *J. Phys. Chem. Lett.* **2010**, *1*, 3039–3045.

[167] Fuke, N.; Hoch, L. B.; Koposov, A. Y.; Manner, V. W.; Werder, D. J.; Fukui, A.; Koide, N.; Katayama, H.; Sykora, M. *ACS Nano* **2010**, *4*, 6377–6386.

[168] Yu, P.; Zhu, K.; Norman, A. G.; Ferrere, S.; Frank, A. J.; Nozik, A. J. *J. Phys. Chem. B* **2006**, *110*, 25451–25454.

[169] Shen, Q.; Arae, D.; Toyoda, T. *J. Photoch. Photobio. A* **2004**, *164*, 75–80.

[170] Niitsoo, O.; Sarkar, S. K.; Pejoux, C.; Ruhle, S.; Cahen, D.; Hodes, G. *J. Photoch. Photobio. A* **2006**, *181*, 306–313.

[171] Mora-Seró, I.; Bisquert, J.; Dittrich, T.; Belaidi, A.; Susha, A. S.; Rogach, A. L. *J. Phys. Chem. C* **2007**, *111*, 14889–14892.

[172] Kalyuzhny, G.; Murray, R. *J. Phys. Chem. B* **2005**, *109*, 7012–7021.

[173] Hyun, B.; Bartnik, A. C.; Lee, J.; Imoto, H.; Sun, L.; Choi, J. J.; Chujo, Y.; Hanrath, T.; Ober, C. K.; Wise, F. W. *Nano Lett.* **2010**, *10*, 318–323.

[174] Sardar, R.; Heap, T. B.; Shumaker-Parry, J. S. *J. Am. Chem. Soc.* **2007**, *129*, 5356–5357.